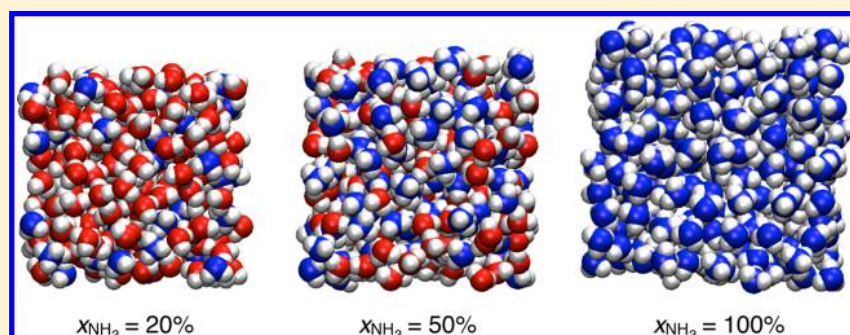


Polarizable Interaction Model for Liquid, Supercritical, and Aqueous Ammonia

Esam A. Orabi[‡] and Guillaume Lamoureux*

Department of Chemistry and Biochemistry and Centre for Research in Molecular Modeling (CERMM), Concordia University, 7141 Sherbrooke Street West, Montréal, Québec H4B 1R6, Canada

S Supporting Information



ABSTRACT: A polarizable model for ammonia is optimized based on the ab initio properties of the NH_3 molecule and the $\text{NH}_3\text{--NH}_3$ and $\text{NH}_3\text{--H}_2\text{O}$ dimers calculated at the MP2 level. For larger $(\text{NH}_3)_m$, $\text{NH}_3(\text{H}_2\text{O})_m$, and $\text{H}_2\text{O}(\text{NH}_3)_n$ clusters ($m = 2\text{--}7$ and $n = 1\text{--}4$), the model yields structural and binding energies in good agreement with ab initio calculations without further adjustments. It also reproduces the structure, density, heat of vaporization, self-diffusion coefficient, heat capacity, and isothermal compressibility of liquid ammonia at the boiling point. The model is further validated by calculating some of these properties at various temperatures and pressures spanning the liquid and supercritical phases of the fluid (up to 700 K and 200 MPa). The excellent transferability of the model suggests that it can be used to investigate properties of fluid ammonia under conditions for which experiments are not easy to perform. For aqueous ammonia solutions, the model yields liquid structures and densities in good agreement with experimental data and allows the nonlinearity in the density-composition plot to be interpreted in terms of structural changes with composition. Finally, the model is used to investigate the solvation structure of ammonia in liquid water and of water in liquid ammonia and to calculate the solvation free energy of NH_3 and H_2O in aqueous ammonia as a function of solution composition and temperature. The simulation results suggest the presence of a transition around 50% molar $\text{NH}_3/\text{H}_2\text{O}$ compositions, above which water molecules are preferably solvated by ammonia.

1. INTRODUCTION

Ammonia is an amphiprotic molecule often described as “water-like,” due to the considerable similarity of its solvent properties to those of water.^{1,2} Both molecules can function as hydrogen bond donor and acceptor and have a comparable ability to dissolve a variety of species such as ionic and molecular compounds and elemental metals and nonmetals.^{1,2} Compared to water, ammonia has a lower dielectric constant, which results in ammonia being generally a poorer solvent for ionic compounds but a better solvent for covalent compounds.² However, the power of ammonia in dissociating electrolytes closely approaches that of water; some salts conduct electricity even better in ammonia than in water.^{1,2} Ammonia is used as a solvent for organic reactions and in many industrial sectors as a refrigerant, fertilizer, cleaner, and precursor to high-energy nitrogenous compounds. In both its neutral (NH_3) and ionic (NH_4^+) forms, it is a source of nitrogen for amino acid synthesis in bacteria and plants, supports the growth of yeast cells, and helps maintain the acid–base equilibrium in mammals.^{3–7}

Ammonia is one of the weakest and simplest hydrogen-bonded liquids.^{8–11} Structural data of liquid ammonia from X-ray^{8,9} and neutron^{10,11} diffraction experiments, as well as abundant experimental data on the physical properties of the fluid (such as density,¹² heat capacity,¹³ self-diffusion coefficient,^{14–16} dielectric constant,¹⁷ viscosity,¹⁸ and heat of vaporization^{13,19}) have prompted computational chemists to develop molecular models for understanding the properties of liquid ammonia. Experimental studies^{20–24} and ab initio investigations^{25–27} of ammonia clusters have also been reported. These studies are important for understanding the structure and stability of the clusters and can provide insight on the transition toward the bulk fluid as the cluster size increases. They also provide useful benchmark data to test and validate new molecular models. The weak nature of the intermolecular interaction in the ammonia dimer^{20–27} suggests however that accurate experiments and high level ab initio calculations might

Received: December 22, 2012

Published: February 26, 2013

be required for reliable determination of the structure and binding energy in ammonia clusters.

A number of intermolecular potentials have been used to explore the structure and binding energies of $(\text{NH}_3)_m$ ammonia clusters.^{28–32} Sagarik et al. have developed a pairwise-additive potential to calculate the structure and interaction energies of the ammonia dimer and to compute static and dynamic properties of liquid NH_3 .²⁸ This potential was used by Greer et al. to investigate ammonia clusters with $m = 3–7$.²⁹ Using the rigid-ammonia pairwise-additive model of Impey and Klein,³³ Beu and Buck³⁰ have performed geometry optimization and binding energy calculations of clusters with $m = 2–18$. Using a rigid-ammonia model with an explicit description of induction parametrized by fitting to ab initio data, Janeiro-Barral et al.³¹ have investigated the structure and energetics of ammonia clusters with $m = 2–20$. Yu and Yang³² have used an eight-point intermolecular potential including fluctuating charges and flexible bonds to study the structure, binding energies, and vibrational frequencies of ammonia clusters with $m = 1–5$ and to explore the dynamical properties of liquid ammonia. Although binding energies calculated with both nonpolarizable^{28–30} and polarizable^{31,32} models have comparable performance relative to ab initio results, the contributions of nonadditive effects such as induction forces are important for providing more accurate total interaction energies.^{31,32} Almeida et al.³⁴ have investigated the electronic properties of ammonia clusters electrostatically embedded in liquid ammonia (sampled using the Impey and Klein potential) and found a 27% increase in the average dipole moment of liquid ammonia compared to the gas-phase value, suggesting again the importance of induction forces.

Over past decades, several theoretical studies^{28,32,33,35–51} have contributed to molecular-level understanding of the structure, thermodynamics, and rheology of fluid ammonia. Different approaches have been used, going from computationally inexpensive simulations using nonpolarizable^{28,33,35–40,44–50} and polarizable^{32,51} force fields to time-consuming quantum mechanical/molecular mechanical (QM/MM)⁴³ and ab initio^{38,40–42} simulations.

Mixtures of ammonia and water have various industrial applications and play an important role in refrigeration and power generation cycles.⁵² The $\text{NH}_3\text{--H}_2\text{O}$ dimer itself represents the simplest system containing an $\text{N}\cdots\text{H}\cdots\text{O}$ hydrogen bond (ubiquitous in biological molecules) and has been the subject of several experimental^{53–57} and theoretical studies.^{58–63} Experimental investigations on mixtures of the two fluids have similarly been performed.^{8,64,65} Using X-ray scattering experiments, Narten⁸ has reported the structure of aqueous ammonia solutions with two compositions ($x_{\text{NH}_3} = 18.3$ and 28.5%) at 4 °C. Ammonia adsorption at the air–water interface⁶⁴ and its adsorption on and diffusion into ice⁶⁵ have also been studied experimentally. A number of theoretical studies have been performed to investigate the solvation of ammonia in water clusters^{61,64,66–68} and the properties of aqueous ammonia and its liquid/vapor interface.^{36,51,69–77}

With a few exceptions,^{37,44,46–50} most studies have so far focused on fluid ammonia under a limited range of thermodynamic conditions (around standard temperature and pressure), and few potential models have been used to study aqueous ammonia solutions.^{73–76} Although in principle ab initio simulations are expected to provide the best description of fluid properties, a reliable sampling of the configuration

space requires long simulations using highly correlated ab initio methods, which are computationally prohibitive. Potential models that reproduce various experimental properties under different thermodynamic conditions, especially those for which experiments are difficult to perform, can thus provide a convenient alternative. The fact that polarization has been found essential to modeling cluster and liquid ammonia,^{31,32,34} to reproducing the ab initio properties in ammonia–water clusters,⁶¹ and to reproducing the hydration free energy of NH_3 ⁷⁶ suggests that, for such a purpose, polarizable potential models are preferable to nonpolarizable ones.

In this work, we aim to parametrize a polarizable potential model for NH_3 that can be reliably used to simulate liquid and aqueous ammonia solutions under different thermodynamic conditions. For this purpose, MP2-level geometry optimizations are performed on $(\text{NH}_3)_m$, $\text{NH}_3(\text{H}_2\text{O})_n$, and $\text{H}_2\text{O}(\text{NH}_3)_n$ clusters ($m = 1–7$ and $n = 1–4$). We also calculate various ab initio energy surfaces of the $\text{NH}_3\text{--NH}_3$ and $\text{NH}_3\text{--H}_2\text{O}$ dimers. A polarizable model based on classical Drude oscillators⁷⁸ is then generated for ammonia–ammonia and ammonia–water interactions. The model is parametrized based on the ab initio properties of the NH_3 monomer and its dimers with H_2O and NH_3 . The model is validated by calculating the structure and interaction energies of the larger clusters and by simulating properties of fluid ammonia at temperatures and pressures for which experimental data are available. It is then used to calculate the hydration structure and hydration free energy of ammonia and to explore the properties of aqueous ammonia solutions at various compositions and temperatures.

2. METHODS

2.1. Ab Initio Calculations. Ab initio calculations on $(\text{NH}_3)_m$, $\text{NH}_3(\text{H}_2\text{O})_n$, and $\text{H}_2\text{O}(\text{NH}_3)_n$ clusters ($m = 1–7$ and $n = 1–4$) are carried out at the MP2/6-311++G(d,p) level with frozen-core (FC) electrons, using the Gaussian 09 program.⁷⁹ Calculations at the MP2(full)/6-311++G(d,p) level give almost the same results as FC calculations. Except for the transition state structures of the $\text{NH}_3\text{--NH}_3$ and $\text{NH}_3\text{--H}_2\text{O}$ dimers and the $\text{O}\cdots\text{H}\cdots\text{N}$ hydrogen-bonded $\text{NH}_3\text{--H}_2\text{O}$ dimer, geometry optimizations are carried out without imposing any symmetry constraints. Frequency calculations are performed on all resulting structures to confirm that they are energy minima. Interaction energies are corrected for basis set superposition error (BSSE) using the counterpoise (CP) procedure proposed by Boys and Bernardi.⁸⁰ For the ammonia monomer, geometry optimization and frequency calculations are also performed using coupled cluster theory with single, double, and perturbative triple excitations (CCSD(T)) on 6-311++G(d,p), 6-311++G(2d,2p), and Dunning's aug-cc-pV5Z⁸¹ basis sets. In order to assess the accuracy of the MP2 results, the minimum energy and transition state conformers in the $\text{NH}_3\text{--NH}_3$ and $\text{NH}_3\text{--H}_2\text{O}$ dimers are also optimized at the CCSD(T)/6-311++G(d,p) and CCSD(T)/6-311++G(2d,2p) levels.

For the $\text{NH}_3\text{--NH}_3$ dimer (see Figure 1), potential energy surfaces (PESSs) are generated by scanning the following parameters in the eclipsed isomer (Figure 1a): $\text{N}\cdots\text{N}$ distance (from 2 to 8 Å), $\text{N}\cdots\text{N}\cdots\text{H}$ angle (from 20 to 160°), and $\text{H}\cdots\text{N}\cdots\text{N}\cdots\text{H}$ dihedral (from 0 to 180°). The bond angle scan describes deviations from the optimal orientation of one molecule relative to the other, and the dihedral scan describes the relative orientation of hydrogen atoms in the two molecules, going from the eclipsed to the staggered configurations. For the $\text{NH}_3\text{--H}_2\text{O}$ dimer (see Figure 2),

PESs are generated by scanning the N...O distance in the N...H–O and O...H–N hydrogen-bonded complexes (from 2.0 to 8.0 Å), the N...O–H angle in the N...H–O hydrogen-bonded complex (from 30 to 180°), and the N...H–O–H dihedral in the N...H–O hydrogen-bonded complex (from 0 to 180°). As for the ammonia dimer, the angle and dihedral scans target the position and hydrogen atoms' orientations in the two molecules. All curves are computed at the MP2(FC)/6-311++G(d,p) level with rigid monomers maintained in their gas-phase optimal geometries and are corrected for BSSE.

2.2. Molecular Mechanical Calculations. Molecular mechanics (MM) calculations are performed with the program CHARMM.⁸² Electronic polarization is described using the classical Drude oscillator model.⁷⁸ The ammonia model is calibrated based on the ab initio MP2(FC)/6-311++G(d,p) properties of the ammonia monomer, ammonia dimer, and ammonia–water dimer. The polarizable SWM4-NDP water model⁸³ is used in all MM calculations involving water.

2.2.1. Potential Energy Function and Parametrization Strategy. Molecular polarizability is implemented by attaching a light (0.4 amu) charged particle to all heavy (non-hydrogen) atoms via a harmonic spring with force constant $k_D = 1000$ kcal/mol/Å².⁷⁸ The partial charge q of a polarizable atom is then distributed between the Drude particle (q_D) and the atom core ($q_c = q - q_D$) with the Drude particle charge being determined from the atomic polarizability via the relation $\alpha = q_D^2/k_D$. A separation d between the Drude particle and the polarizable atom results in an induced dipole moment $q_D d$. To account for induction, the functional form of the CHARMM additive empirical potential energy⁸⁴ is modified to include electrostatic interactions with the Drude oscillators. A term describing the self-energy of a polarizable atom ($k_D d^2/2$) is also added.^{78,85} Similarly to our recently developed polarizable model for NH₄⁺,⁸⁵ NH₃ is modeled by four atomic sites and an auxiliary Drude particle attached to the nitrogen atom. The polarizable potential energy function that describes the interaction energy in liquid and aqueous ammonia solutions can be written as follows:^{78,84,85}

$$\begin{aligned}
 U(R) = & \sum_{i=1}^N \frac{1}{2} k_D |\mathbf{r}_i - \mathbf{r}_{Di}|^2 + \sum_{\text{HNH angles}} k_\theta (\theta - \theta_0)^2 \\
 & + \sum_{\text{nonbond}} E_{\min,ij} \left[\left(\frac{R_{\min,ij}}{|\mathbf{r}_i - \mathbf{r}_j|} \right)^{12} - 2 \left(\frac{R_{\min,ij}}{|\mathbf{r}_i - \mathbf{r}_j|} \right)^6 \right] \\
 & + \sum_{\text{nonbond}} \left(\frac{q_i q_j}{|\mathbf{r}_i - \mathbf{r}_j|} + \frac{q_{Di} q_{Dj}}{|\mathbf{r}_{Di} - \mathbf{r}_{Dj}|} + \frac{q_i q_{Dj}}{|\mathbf{r}_i - \mathbf{r}_{Dj}|} \right. \\
 & \left. + \frac{q_{Di} q_{Dj}}{|\mathbf{r}_{Di} - \mathbf{r}_{Dj}|} \right) \quad (1)
 \end{aligned}$$

where N is the number of interacting molecules and \mathbf{r}_i and \mathbf{r}_{Di} are the positions of the core particle i and its corresponding Drude particle, respectively. k_θ , θ , and θ_0 are respectively the force constant, instantaneous value, and equilibrium value for the HNH angles. q_i is the partial charge on the core particles i , and q_{Di} is the partial charge of its Drude particle. $E_{\min,ij}$ and $R_{\min,ij}$ are the mixed Lennard-Jones (LJ) parameters between nonbonded atoms i and j , defined by the Lorentz–Berthelot combination rules:

$$E_{\min,ij} = \sqrt{E_{\min,i} \times E_{\min,j}} \text{ and } R_{\min,ij} = \frac{R_{\min,i} + R_{\min,j}}{2} \quad (2)$$

The potential energy term that describes deviations in bonds:

$$E_{\text{bond}} = \sum_{\text{bonds}} k_b (b - b_0)^2 \quad (3)$$

where k_b , b , and b_0 are the force constant, instantaneous length, and equilibrium length for NH and OH bonds, is not included in eq 1 because these bonds are constrained to their equilibrium lengths in all MM calculations using the SHAKE/Roll-RATTLE/Roll algorithm.⁸⁶ Water is described using the polarizable SWM4-NDP model, in which the HOH angle is rigid⁸³ and thus excluded from the angle-bending term of eq 1.

The equilibrium bonded parameters for NH₃ (b_0 for NH bonds and θ_0 for HNH angles) are based on MP2(FC)/6-311++G(d,p) optimization of the monomer. The bond and angle force constants, k_b and k_θ , are set to reproduce the ab initio vibration frequencies of the monomer and to minimize distortions in its pyramidal structure during molecular dynamics (MD) simulations.⁸⁵ The electrostatic parameters (partial atomic charges and polarizability) are similarly based on the ab initio properties of the NH₃ monomer, with the partial atomic charges on N and H atoms fitted to reproduce the MP2 dipole moment and the polarizability of the N atom calculated from the trace of the MP2 polarizability tensor.⁸⁵

Optimization of the polarizable model for ammonia–ammonia and ammonia–water interactions follows our previous approach.⁸⁵ In particular, the model is optimized based on the ab initio properties (complexation energies and PESs) of the dimers. The “generic” LJ parameters of N and H of NH₃ are optimized based on the properties of the ammonia–water complex. The ammonia dimer’s potential model is adjusted by optimizing pair-specific LJ parameters between N atoms, introduced via the NBFIX⁸² facility of CHARMM. Following our previously reported parametrization approach,⁸⁵ optimization of the atomic and pair-specific LJ parameters initially targets the ab initio PESs of the two dimers. Each point of the energy surfaces contributes to the error function χ^2 to be minimized by a Boltzmann-weighted error term.⁸⁵ Since the PESs are computed using the rigid monomer geometries of H₂O and NH₃, parameters obtained from the minimization of χ^2 are further refined to reproduce the complexation energies of the fully relaxed ab initio dimers.⁸⁵ This slight modification of the parameters improves the complexation energy of the dimers, but creates small deviations in the position of the energy minimum on the rigid-monomer PESs.

2.2.2. Molecular Dynamics. Most previously published computational studies on liquid ammonia are artificially imposing the experimental density by performing simulations in the canonical (NVT)^{28,32,33,35,38–40,43,47,50,51} or the microcanonical (NVE)^{34,42,45,46} ensembles for which the volume of the system corresponds to the experimental density of the liquid at the studied thermodynamic conditions. By contrast, all MD simulations reported in this work are performed in the isothermal–isobaric ensemble (NPT). Unless otherwise specified, the total number of molecules (ammonia and/or water) is 250 in each system. All simulations are performed with cubic periodic boundary conditions using a previously reported simulation protocol.⁸⁵ The SWM4-NDP polarizable

Table 1. Properties of the Ammonia Monomer Calculated at Various ab Initio Levels and Corresponding Experimental Values^a

| property | MP2(FC)/6-311+ +G(d,p) | CCSD(T)/6-311+ +G(d,p) | CCSD(T)/6-311+ +G(2d,2p) | CCSD(T)/aug-cc- pV5Z | Drude | expt. |
|---|---------------------------|---------------------------|-----------------------------|-------------------------|--------|---------------------|
| NH bond (Å) | 1.0135 | 1.0167 | 1.0120 | 1.0122 | 1.0135 | 1.0124 ^b |
| HNH angle (deg) | 107.29 | 106.84 | 106.69 | 106.60 | 107.29 | 106.67 ^b |
| HNHH dihedral (deg) | 114.03 | 114.13 | 113.74 | 113.56 | 114.03 | 112.15 ^b |
| dipole (D) | 1.782 | 1.808 | 1.682 | 1.622 | 1.782 | 1.561 ^c |
| vibration frequencies (cm ⁻¹) | | | | | | |
| ν_1 | 3530 | 3485 | 3491 | 3479 | 3556 | 3337 ^d |
| ν_2 | 1069 | 1094 | 1086 | 1056 | 1614 | 950 ^d |
| ν_3 | 3681 | 3621 | 3613 | 3611 | 3667 | 3444 ^d |
| ν_4 | 1665 | 1662 | 1693 | 1674 | 2218 | 1627 ^d |

^aValues from the optimized Drude model are also given (see section 3.3). ^bRef 91. ^cRef 92. ^dRef 93.

water model⁸³ is used for simulations of aqueous ammonia. Electrostatic interactions are computed using the particle-mesh Ewald method⁸⁷ with $\kappa = 0.34$ for the charge screening and a 1.0 Å grid spacing with fourth-order splines for the mesh interpolation. The real-space interactions (Lennard-Jones and electrostatic) are cut off at 15 Å and the long-range contribution from the Lennard-Jones term is introduced as an average density-dependent term.⁸⁸ The temperature of the system is controlled with a two-thermostat algorithm, where atoms are kept at the desired temperature and auxiliary Drude particles are kept at a low temperature (1 K) to ensure self-consistent dipole induction.⁷⁸ The equations of motion are integrated using a 1 fs time step, with all bonds involving hydrogen atoms kept at their reference lengths using the SHAKE/Roll-RATTLE/Roll algorithm.⁸⁶

2.2.3. Free Energy Calculations. The optimized polarizable potential model for ammonia–water interaction is validated by calculating the hydration free energy of NH₃ at $T = 298.15$ K and $p = 1$ atm = 0.1013 MPa. The hydration free energy of H₂O relative to NH₃ in bulk water ($\Delta\Delta G_{\text{hyd}} = \Delta G_{\text{hyd}}(\text{H}_2\text{O}) - \Delta G_{\text{hyd}}(\text{NH}_3)$) is calculated using a previously reported thermodynamic integration approach.⁸⁵ Specifically, we use a special hybrid residue in which virtual NH₃ and H₂O groups are linked through their heavy atoms via a weak harmonic bond of force constant 5 kcal/mol/Å².⁸⁵ This residue is composed of one original “real” molecule linked to a “dummy” molecule having no interactions with the real particles (apart from the harmonic tether). The relative solvation free energy is evaluated from the conventional thermodynamic cycle for solute transformation

$$\begin{aligned}\Delta\Delta G_{\text{hyd}} &= \Delta G_{\text{hyd}}(\text{H}_2\text{O}) - \Delta G_{\text{hyd}}(\text{NH}_3) \\ &= \Delta G_{\text{mut}}^{\text{aq}}(\text{NH}_3 \rightarrow \text{H}_2\text{O})\end{aligned}\quad (4)$$

where $\Delta G_{\text{mut}}^{\text{aq}}$ is the relative free energy for the alchemical solute NH₃ → H₂O “mutation” performed in water. The transformation is performed in 17 steps, controlled by a scaling parameter λ which takes the following values: 0, 0.005, 0.02, 0.04, 0.1, 0.2, 0.3, 0.4, 0.5, 0.6, 0.7, 0.8, 0.9, 0.96, 0.98, 0.995, and 1. Each λ window is equilibrated for 150 ps followed by subsequent data collection for 350 ps. Each mutation is performed in the forward and backward directions in six independent replicates in order to confirm the convergence and estimate the error in the calculated values.

The solvation free energy of H₂O and NH₃ in aqueous ammonia is calculated as a function of the mixture composition and temperature. For this purpose, we initially calculate the solvation free energy of H₂O, $\Delta G_{\text{solv}}(\text{H}_2\text{O})$, by mutating one

water molecule into a dummy molecule, having no charges and no LJ parameters, using free energy perturbation (FEP) theory. The transformation is performed in 21 steps with the scaling parameter λ taking the values 0, 0.00001, 0.0001, 0.001, 0.01, 0.05, 0.1, 0.2, 0.3, 0.4, 0.5, 0.6, 0.7, 0.8, 0.9, 0.95, 0.99, 0.999, 0.9999, 0.99999, and 1. A slow growth of λ near its extreme values is used to avoid sampling errors created by the sudden appearance or disappearance of the solute. This integration scheme is equivalent to the previously reported free energy perturbation protocol, in which the solvation free energy is decomposed into three components, each being calculated from independent simulations:^{89,90}

$$\Delta G_{\text{solv}} = \Delta G_{\text{elec}} + \Delta G_{\text{disp}} + \Delta G_{\text{rep}} \quad (5)$$

where ΔG_{elec} is the electrostatic component of the solvation free energy and ΔG_{disp} and ΔG_{rep} are the attractive (dispersive) and repulsive components of the LJ interaction. Our preliminary tests show that the integration scheme yields hydration free energy of water (−5.9 kcal/mol) and alkali ions (−109.6 kcal/mol for Li⁺, −85.4 kcal/mol for Na⁺, −68.1 kcal/mol for K⁺, −63.2 kcal/mol for Rb⁺, and −56.1 kcal/mol for Cs⁺) in excellent agreement with the results from the decomposition scheme of eq 5 (−5.9 kcal/mol for H₂O⁸³ and −109.8, −85.6, −67.9, −63.0, and −55.8 kcal/mol for Li⁺, Na⁺, K⁺, Rb⁺, and Cs⁺, respectively⁹⁰). To reduce the computing effort associated with having that many λ values, the solvation free energy of NH₃ is calculated relative to that of H₂O:

$$\Delta G_{\text{solv}}(\text{NH}_3) = \Delta G_{\text{solv}}(\text{H}_2\text{O}) - \Delta\Delta G_{\text{solv}} \quad (6)$$

The solvation free energy calculations are performed in aqueous ammonia solutions composed of a total of 251 molecules (one solute + 250 solvent molecules), with various ammonia mole fractions, $0.0 \leq x_{\text{NH}_3} \leq 1.0$. The simulations are performed at three temperatures, $T = 239.8$, 273.15, and 298.15 K, and at the corresponding vapor pressures of liquid ammonia, $p = 0.1013$, 0.4294, and 1.0030 MPa.

3. RESULTS AND DISCUSSION

3.1. Ab Initio Optimized Geometries. The enumeration of all stable conformers of (NH₃)_{*m*} and NH₃(H₂O)_{*n*} clusters is outside the scope of this study and can be found elsewhere.^{26,27,61,64,66–68} Except for the dimers ($m = 2$, $n = 1$), only the minimum-energy conformers of these clusters are considered, solely for the purpose of validating the NH₃ potential model. However, since to the best of our knowledge no ab initio investigations have been reported on H₂O(NH₃)_{*n*}

clusters larger than the trimer ($n = 2$), we report all stable conformers we have identified in clusters with $n = 1-4$.

3.1.1. Ammonia Monomer. The MP2(FC)/6-311++G(d,p), CCSD(T)/6-311++G(d,p), CCSD(T)/6-311++G(2d,2p), and CCSD(T)/aug-cc-pV5Z optimized geometries, gas-phase dipole moments, and vibrational frequencies of the isolated ammonia molecule are reported in Table 1. The calculated internal geometry of ammonia at the MP2 level shows $r_{\text{NH}} = 1.0135 \text{ \AA}$ and $\theta_{\text{H-N-H}} = 107.29^\circ$, in good agreement with the experimental data⁹¹ ($r_{\text{NH}} = 1.0124 \text{ \AA}$, $\theta_{\text{H-N-H}} = 107.67^\circ$) and the higher-level calculations results. The MP2-optimized structure possesses a dipole moment of 1.782 D, comparable to the CCSD(T)/6-311++G(d,p) value (1.808 D) but larger than the CCSD(T)/6-311++G(2d,2p) value (1.682 D), the CCSD(T)/aug-cc-pV5Z value (1.622 D), and the experimental gas-phase value (1.561 D).⁹² Table 1 also shows that frequencies calculated at the MP2 level are close to the experimental⁹³ and CCSD(T) values.

3.1.2. $(\text{NH}_3)_m$ ($m = 2-7$) Clusters. Figure 1 shows structures of the $(\text{NH}_3)_m$ clusters ($m = 2-7$) obtained from geometry

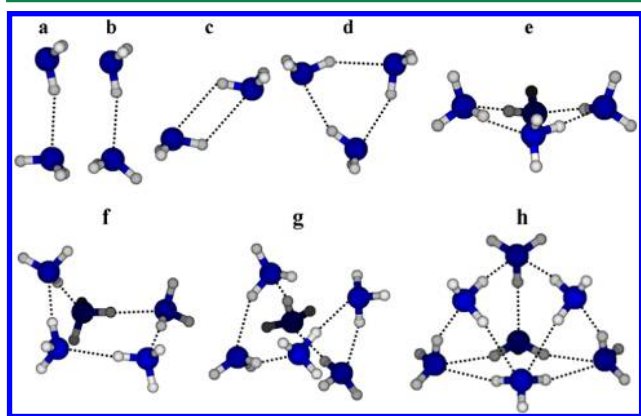


Figure 1. Geometries of ammonia clusters optimized at the MP2(FC)/6-311++G(d,p) level: (a) eclipsed dimer, (b) staggered dimer, (c) cyclic dimer (transition state), (d) trimer, (e) tetramer, (f) pentamer, (g) hexamer, and (h) heptamer.

optimization at the MP2(FC)/6-311++G(d,p) level. Table 2 lists the intermolecular structural properties and the interaction energies of three structures of the dimer, with and without correction for BSSE (E^{CP} and E , respectively). Table 3 reports the MP2 interaction energies of the clusters and the corresponding energies calculated with the optimized Drude model (see section 3.3), along with literature data from ab initio calculations, empirical potential functions, and experiments.

Geometry optimizations of the dimer show that both the eclipsed and staggered isomers (Figure 1a and b, respectively) are stable and that the doubly hydrogen-bonded cyclic dimer

(Figure 1c) is a first-order transition state (TS), in accord with previous ab initio results.^{25,27} The very weak stability of the eclipsed isomer relative to the staggered one (0.05 kcal/mol at the MP2 level) is consistent with a very low rotation barrier of the hydrogen bond acceptor about its C_3 axis.²⁵

The counterpoise procedure appears to overestimate the BSSE of some conformers, and yields E^{CP} values lower for the TS structure (Figure 1c) than for some of the stable isomers (see Table 2). For instance the MP2(FC)/6-311++G(d,p) calculations show a BSSE of 0.77 kcal/mol for the TS structure, compared to 1.07 kcal/mol for the eclipsed isomer and 1.12 kcal/mol for the staggered one. On the other hand, the eclipsed isomer is 0.05 kcal/mol more stable than the TS structure at the CCSD(T)/6-311++G(2d,2p) level, which represents an energy barrier to proton donor–acceptor interchange comparable to the 0.02 kcal/mol value reported by Lee and Park at the MP2/aug-cc-pVQZ//MP2/aug-cc-pVTZ level²⁵ and the 0.007 kcal/mol value reported by Janeiro-Barral and Mella at the MP2/aug-cc-pVQZ level.²⁷

Table 2 shows good agreement between the structural and energetic properties of the minimum-energy isomer at the MP2 and CCSD(T) levels, with discrepancies of at most 0.11 kcal/mol for binding energies, 0.024 Å for N...N distances, and 3.6° for N...H–N angles. The MP2 binding energy of the dimer, $E^{\text{CP}} = -2.73$ kcal/mol, is in agreement with the experimentally reported infrared photodissociation energies of the dimer (2.57–3.15 kcal/mol,²⁰ < 2.8 kcal/mol,²¹ and < 2.72 kcal/mol²²). The overall good agreement between the monomer and dimer properties calculated at the MP2 level and those calculated at the higher CCSD(T) level suggests that the MP2(FC)/6-311++G(d,p) level of theory is suitable for studying ammonia clusters.

The lowest-energy conformation of the trimer is a C_{3h} -symmetric cyclic isomer (Figure 1d), in agreement with previous ab initio results.^{26,27} The N...N separation in the trimer is 3.173 Å, significantly shorter than the distance observed in the minimum-energy dimer (3.258 Å). This shortening indicates binding cooperativity: despite the frustration induced in the individual hydrogen bonds, each dimer is strengthened upon binding of a third NH_3 molecule.

The most stable ammonia tetramer is a cyclic “boat” structure²⁷ (Figure 1e) with a binding energy $E^{\text{CP}} = -14.17$ kcal/mol. Molecules in direct contact are separated by an equal N...N distance of 3.160 Å, which is 0.013 Å shorter than in the trimer.

The most stable pentamer is a nonplanar cyclic structure^{26,27} with four quasi-planar ammonia molecules and a fifth molecule above the plane (Figure 1f). The CP-corrected interaction energy of the complex is -17.88 kcal/mol, and the N...N separation between H-bonded ammonia molecules varies between 3.145 Å and 3.171 Å.

Table 2. Intermolecular Geometrical Parameters, $r_{\text{N}\cdots\text{N}}$ (Å) and $\angle\text{N}\cdots\text{H}-\text{N}$ (deg), and Interaction Energies with and without Correction for BSSE (E^{CP} and E , respectively, in kcal/mol) for the Three Structures of the Ammonia Dimer (a, eclipsed; b, staggered; c, cyclic TS), Optimized at the MP2 and CCSD(T) Levels of Theory

| structure | MP2(FC)/6-311++G(d,p) | | | | CCSD(T)/6-311++G(d,p) | | | | CCSD(T)/6-311++G(2d,2p) | | | |
|-----------|-----------------------|-----------------|------------------------------|---|-----------------------|-----------------|------------------------------|---|-------------------------|-----------------|------------------------------|---|
| | E | E^{CP} | $r_{\text{N}\cdots\text{N}}$ | $\angle\text{N}\cdots\text{H}-\text{N}$ | E | E^{CP} | $r_{\text{N}\cdots\text{N}}$ | $\angle\text{N}\cdots\text{H}-\text{N}$ | E | E^{CP} | $r_{\text{N}\cdots\text{N}}$ | $\angle\text{N}\cdots\text{H}-\text{N}$ |
| a | −3.80 | −2.73 | 3.258 | 165.5 | −3.74 | −2.62 | 3.277 | 167.0 | −3.28 | −2.81 | 3.282 | 161.9 |
| b | −3.80 | −2.68 | 3.261 | 167.4 | −3.74 | −2.61 | 3.264 | 165.4 | −3.21 | −2.70 | 3.304 | 165.8 |
| c | −3.55 | −2.78 | 3.172 | 121.6 | −3.52 | −2.68 | 3.181 | 121.4 | −3.17 | −2.76 | 3.195 | 121.7 |

Table 3. Uncorrected (E) and CP-Corrected (E^{CP}) Binding Energies of the $(\text{NH}_3)_m$ Clusters ($m = 2-7$) Calculated at the MP2(FC)/6-311++G(d,p) Level Compared with Computational and Experimental Data from the Literature (All Energies in kcal/mol)

| m | ab initio | | | | potential models | | | | | expt. ^h |
|------|-----------|------------------|--|---|---------------------------|---------------------------|------------------------------------|--------------------------|---------------------|---|
| | E^a | $E^{\text{CP}a}$ | Kulkarni and Pathak (E) ^b | Janeiro-Barral and Mella (E^{CP}) ^c | Greer et al. ^d | Beu and Buck ^e | Janeiro-Barral et al. ^f | Yu and Yang ^g | $E^{\text{Drude}a}$ | |
| 2(a) | -3.80 | -2.73 | -4.03 | -2.74 | | -2.78 | | -2.93 | -2.64 (0.045) | 2.57–3.15 ⁱ , < 2.8 ^j |
| 2(b) | -3.80 | -2.68 | | | | | | | -2.63 (0.025) | < 2.72 ^k , 2.77 ^l |
| 2(c) | -3.55 | -2.78 | | -2.74 | | | | -2.92 | -2.40 (0.190) | |
| 3 | -12.31 | -9.34 | -13.02 | -9.24 | -8.44 | -8.26 | -9.06 | -9.76 | -8.13 (0.403) | |
| 4 | -19.32 | -14.17 | -20.12 | -14.30 | -13.10 | -12.62 | -14.91 | -15.12 | -13.24 (0.233) | |
| 5 | -24.66 | -17.88 | -25.48 | -18.16 | -16.93 | -16.72 | -19.45 | -18.91 | -17.30 (0.116) | |
| 6 | -31.32 | -22.56 | -31.90 ^m | | -22.74 ^m | -22.70 ^m | -24.29 ^m | | -22.11 (0.075) | |
| 7 | -38.91 | -28.27 | | | -28.55 | -28.22 | -30.14 | | -28.50 (-0.033) | |

^aThis work. Values in parentheses represent the error per molecule compared to E^{CP} , calculated as $(E^{\text{Drude}} - E^{\text{CP}})/m$. ^bRef 26, at the MP2/6-31++G(d,p) level and uncorrected for BSSE. ^cRef 27, at the MP2/aug-cc-pVDZ level and corrected for BSSE. ^dRef 29, using an additive rigid potential model. ^eRef 30, using an additive rigid potential model. ^fRef 31, using a rigid-polarizable potential model. ^gRef 32, using the ABEEM ammonia-8P potential. ^hExperimental data are not for a specific dimer geometry. ⁱInfrared photodissociation energy from ref 20. ^jInfrared photodissociation energy from ref 21. ^kInfrared photodissociation energy from ref 22. ^lDissociation energy using threshold photoelectron photoion coincidence time-of-flight method.²³ ^mBinding energy refers to a conformer different from the one reported in this study.

Kulkarni and Pathak²⁶ have reported cyclic and chairlike conformers as the two most stable hexamers, with CP-uncorrected binding energies (E) of -31.90 and -30.96 kcal/mol, respectively (calculated at the MP2/6-31++G(d,p) level). Model potential studies on the hexamer however have suggested various other nonsymmetric conformations as global minima.²⁹⁻³¹ Our MP2 calculations suggest the minimum-energy hexamer to be a C_1 -symmetry conformation with distorted tetragonal bipyramidal geometry (Figure 1g). This conformer possesses a binding energy $E^{\text{CP}} = -22.56$ kcal/mol, 0.45 and 0.99 kcal/mol lower than the cyclic and chairlike hexamers optimized at the same level (structures not shown).

Similarly to previous potential models results,²⁹⁻³¹ the global energy minimum of the heptamer is a C_s symmetrical isomer (Figure 1h) with a binding energy $E^{\text{CP}} = -28.27$ kcal/mol.

3.1.3. $\text{NH}_3(\text{H}_2\text{O})_n$ ($n = 1-4$) Clusters. Figure 2 shows the geometries for ammonia in complex with one to four water

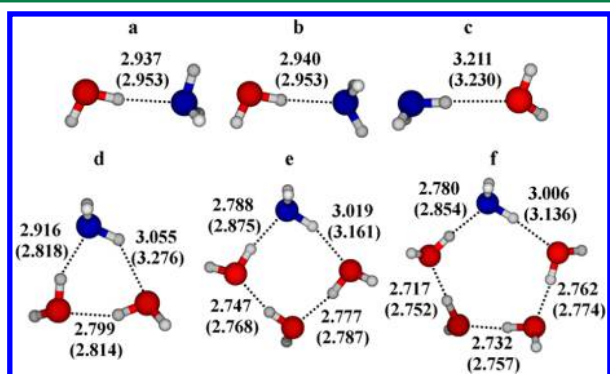


Figure 2. Geometries of $\text{NH}_3(\text{H}_2\text{O})_n$ ($n = 1-4$) clusters optimized at the MP2(FC)/6-311++G(d,p) level. Numbers represent $r_{\text{O}\cdots\text{O}}$ and $r_{\text{N}\cdots\text{O}}$ distances (in Å) for the ab initio optimal structures and in brackets for the Drude model optimal geometries (see section 3.3).

molecules optimized at the MP2(FC)/6-311++G(d,p) level. The corresponding ab initio binding energies are reported in Table 4. As for the ammonia dimer, MP2 calculations on the $\text{NH}_3\text{--H}_2\text{O}$ dimer are compared to CCSD(T)/6-311++G(d,p) and CCSD(T)/6-311++G(2d,2p) calculations.

Table 4. Uncorrected (E) and CP-Corrected (E^{CP}) Binding Energies of the $\text{NH}_3(\text{H}_2\text{O})_n$ ($n = 1-4$) Clusters at MP2(FC)/6-311++G(d,p) Level in Comparison with Drude Models and Literature ab Initio Data (all energies are in kcal/mol)

| n | this work | | | literature |
|------|-----------|-----------------|--------------------|---|
| | E | E^{CP} | E^{Drude} | |
| 1(a) | -7.46 | -5.89 | -5.68 | -5.99, ^a -6.17, ^b -6.30, ^c -6.37, ^d -5.99, ^e -6.33, ^f -6.03 ^g |
| 1(b) | -7.43 | -5.88 | -5.68 | -6.17, ^b -6.36 ^d |
| 1(c) | -3.22 | -2.09 | -2.38 | |
| 2 | -18.06 | -14.12 | -13.06 | -15.52 ^d |
| 3 | -30.10 | -23.00 | -22.60 | -21.35 ^h |
| 4 | -41.29 | -31.27 | -30.81 | -29.00 ^h |

^aRef 58 CP-corrected binding energy calculated at the MP2/TZ2P level. ^bRef 59 CP-corrected binding energies calculated at MP2/aug-cc-pVTZ//CCSD(T)/aug-cc-pVTZ level. ^cRef 60 CP-corrected binding energy at the MP2/cc-pVSZ level. ^dRef 61 CP-corrected binding energies at the MP2/aug-cc-pVTZ level. ^eRef 62 CP-corrected binding energy at the MP2/6-31G* level. ^fRef 63 CP-corrected binding energy at the CCSD(T)/aug-cc-pVQZ level. ^gRef 64 CP-corrected binding energy at the MP2/6-61G(d,p)//MP4SDTQ/6-311++G(3df,2pd) level. ^hRef 66 Binding energies corrected for zero-point energy at the MP2/6-311+G(d,p) level but uncorrected for BSSE.

The minimum-energy isomer of the ammonia–water dimer possesses a trans $\text{N}\cdots\text{H}\cdots\text{O}$ hydrogen-bonded structure (Figure 2a; $E^{\text{CP}} = -5.89$ kcal/mol). The cis conformer (Figure 2b) is a first order TS with a binding energy $E^{\text{CP}} = -5.88$ kcal/mol. The 0.01 kcal/mol difference between the cis and trans isomers represents the barrier height to internal rotation of NH_3 around its C_3 axis and is in agreement with microwave and far-infrared experimental results (0.03 ± 0.001 kcal/mol).⁵⁴ The third structure reported for the dimer (Figure 2c) is an unstable $\text{O}\cdots\text{H}\cdots\text{N}$ hydrogen-bonded structure obtained from an optimization in which the $\text{O}\cdots\text{H}\cdots\text{N}$ angle is constrained at 180° . It is 3.80 kcal/mol less stable than the $\text{N}\cdots\text{H}\cdots\text{O}$ bonded dimer, showing that ammonia is a better H-bond acceptor than donor.⁵³⁻⁵⁷ The $\text{N}\cdots\text{O}$ separation is 2.937 Å in conformer a, 2.940 Å in conformer b, and 3.211 Å in conformer c. The

$\text{N}\cdots\text{H}-\text{O}$ angle is 171° in both isomers a and b, indicating a nonlinear hydrogen bond in agreement with experimental results.⁵⁴ Optimization of conformer a at the CCSD(T)/6-311++G(d,p) level shows an $\text{N}\cdots\text{O}$ distance of 2.955 Å, an $\text{N}\cdots\text{H}-\text{O}$ angle of 171° , and $E^{\text{CP}} = -5.90$ kcal/mol, while optimization at the CCSD(T)/6-311++G(2d,2p) level shows an $\text{N}\cdots\text{O}$ distance of 2.958 Å, an $\text{N}\cdots\text{H}-\text{O}$ angle of 171° , and $E^{\text{CP}} = -5.95$ kcal/mol, in good agreement with the MP2 results. The MP2-calculated binding energy and structural parameters of the global minimum isomer are also in good agreement with Lane et al. calculations at the CCSD(T)/aug-cc-pVQZ level ($r_{\text{N}\cdots\text{O}} = 2.938$ Å, $\angle\text{N}\cdots\text{H}-\text{O} = 170^\circ$, and $E^{\text{CP}} = -6.33$ kcal/mol).⁶³

By comparison, MP2(FC)/6-311++G(d,p) geometry optimization on the water dimer, $(\text{H}_2\text{O})_2$, shows a more linear hydrogen-bonded complex with an $\text{O}\cdots\text{O}$ distance of 2.914 Å, $\text{O}\cdots\text{H}-\text{O}$ angle of 177° , and a binding energy $E^{\text{CP}} = -5.15$ kcal/mol. The water dimer is 0.74 kcal/mol less stable than the ammonia–water dimer, which indicates that ammonia is a better hydrogen bond acceptor than water.

The optimal trimer, tetramer, and pentamer structures are cyclic complexes with two hydrogen bonds per molecule (Figures 2d, e, and f).^{61,64,66–68} Due to the cooperative nature of the interactions, distances between hydrogen-bonded molecules are shorter in larger clusters. For example, the $r_{\text{O}\cdots\text{N}}$ distance for the $\text{N}\cdots\text{H}-\text{O}$ bond is 2.937 Å for the dimer (Figure 2a) but becomes 2.916 Å for the trimer (Figure 2d), 2.788 Å for the tetramer (Figure 2e), and 2.780 Å for the pentamer (Figure 2f). Similarly, the $r_{\text{O}\cdots\text{N}}$ distance for the $\text{O}\cdots\text{H}-\text{N}$ bond goes from 3.211 Å for the constrained dimer (Figure 2c) to 3.006 Å for the pentamer (Figure 2f). The $r_{\text{O}\cdots\text{O}}$ distance follows a similar trend: 2.914 Å for the water dimer (not shown), 2.799 Å for the trimer (Figure 2d), 2.747–2.777 Å for the tetramer (Figure 2e), and 2.717–2.762 Å for the pentamer (Figure 2f).

3.1.4. $\text{H}_2\text{O}(\text{NH}_3)_n$ ($n = 2-4$) Clusters. MP2(FC)/6-311++G(d,p) geometry optimizations are performed on the clusters formed of one water molecule complexed with two, three, and four ammonia molecules. To the best of our knowledge, the only theoretical investigation on $\text{H}_2\text{O}(\text{NH}_3)_n$ clusters larger than the dimer was reported on the $\text{H}_2\text{O}(\text{NH}_3)_2$ complex by Rzepkowska et al.⁶¹ The minimum energy conformers of these clusters are shown in Figure 3. Binding energies are reported in Table 5.

As for the $(\text{NH}_3)_3$ and $\text{NH}_3(\text{H}_2\text{O})_2$ trimers, the minimum-energy conformation of $\text{H}_2\text{O}(\text{NH}_3)_2$ is a cyclic isomer with two

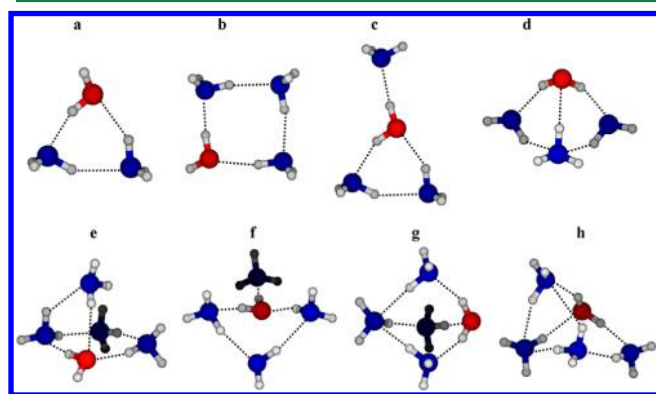


Figure 3. Geometries of $\text{H}_2\text{O}(\text{NH}_3)_n$ ($n = 2-4$) clusters optimized at the MP2(FC)/6-311++G(d,p) level.

Table 5. Uncorrected (E) and CP-Corrected (E^{CP}) Binding Energies of the $\text{H}_2\text{O}(\text{NH}_3)_n$ Clusters ($n = 2-4$) at MP2(FC)/6-311++G(d,p) Level^a

| complex | conformer | E | E^{CP} | E^{Drude} |
|-------------------------------------|-----------|--------|-----------------|--------------------|
| $\text{H}_2\text{O}(\text{NH}_3)_2$ | a | −15.87 | −12.44 | −10.75 |
| | b | −23.99 | −18.18 | −16.66 |
| $\text{H}_2\text{O}(\text{NH}_3)_3$ | c | −21.81 | −16.88 | −15.70 |
| | d | −19.60 | −15.04 | −15.33 |
| | e | −30.10 | −22.41 | −20.80 |
| $\text{H}_2\text{O}(\text{NH}_3)_4$ | f | −29.00 | −21.94 | −21.46 |
| | g | −28.94 | −21.68 | −21.71 |
| | h | −28.19 | −21.23 | −21.15 |

^aBinding energies calculated with the Drude model (E^{Drude}) are also reported. All energies are in kcal/mol.

H-bonds per molecule (Figure 3a). Separations of heavy atoms in the $\text{O}\cdots\text{H}-\text{N}$, $\text{N}\cdots\text{H}-\text{N}$, and $\text{N}\cdots\text{H}-\text{O}$ hydrogen bonds of the trimer are 0.153, 0.126, and 0.099 Å shorter than the corresponding separations in the isolated dimers. In comparison to the calculated value $E^{\text{CP}} = -12.44$ kcal/mol, Rzepkowska et al. have reported a value $E^{\text{CP}} = -13.58$ kcal/mol at the MP2/aug-cc-pvTZ level.⁶¹

Three conformers are optimized for the tetramer (Figures 3b, c, and d), with conformer b being 1.30 kcal/mol more stable than conformer c and 3.14 kcal/mol more stable than conformer d. Structures b and c are quasi-planar and structure d is pyramidal.

Four stable conformations are identified for the pentamer. In the most stable one (Figure 3e), water and three ammonia molecules form a planar cyclic structure, and the fourth, out-of-plane, ammonia molecule acts as a proton donor to water and acceptor to one ammonia molecule. The other pentamer structures (Figures 3f, g, and h) are all characterized by water and three ammonia molecules in “boat” conformations and are respectively 0.47, 0.73, and 1.18 kcal/mol less stable than the global minimum.

3.2. Potential Energy Surfaces. Ab initio potential energy curves for NH_3 in complex with NH_3 and with H_2O are reported as dashed lines in Figure 4, along with the corresponding solid curves calculated with the Drude model (see section 3.3). Three curves are calculated for the ammonia homodimer. Curve 4a is calculated by scanning the $\text{N}\cdots\text{N}$ separation between the two molecules in the eclipsed conformation from 2.0 to 8.0 Å. Curve 4b is calculated by scanning the angle $\text{N}\cdots\text{N}-\text{H}$ from 20° to 160° at the equilibrium $\text{N}\cdots\text{N}$ separation (3.258 Å) and describes the rotation of the hydrogen bond donor molecule in the mirror-symmetry plane of the dimer. Curve 4c is calculated by scanning the dihedral angle $\text{H}-\text{N}\cdots\text{N}-\text{H}$ from 0° to 180° at a $\text{N}\cdots\text{N}$ separation of 3.261 Å and shows the change in energy as the staggered conformer is transformed into the eclipsed one. While the 0° structure corresponds to the exact staggered conformer, the structure at 180° is not the exact eclipsed conformer, which explains the 1.1 kcal/mol difference observed in curve 4c instead of the expected 0.05 kcal/mol (see Table 1). Similarly, three potential energy curves are calculated for the $\text{NH}_3-\text{H}_2\text{O}$ dimer. The first curve (Figure 4d) is calculated by scanning the distance between N and O atoms in both the trans $\text{N}\cdots\text{H}-\text{O}$ and the $\text{O}\cdots\text{H}-\text{N}$ hydrogen-bonded conformers from 2.0 to 8.0 Å. Curve 4e is calculated by scanning the $\text{O}\cdots\text{N}-\text{H}$ angle from 30° to 180° at an $\text{N}\cdots\text{O}$ distance of 2.937 Å. Curve 4f is calculated by scanning the $\text{H}-\text{N}\cdots\text{H}-\text{O}$ dihedral

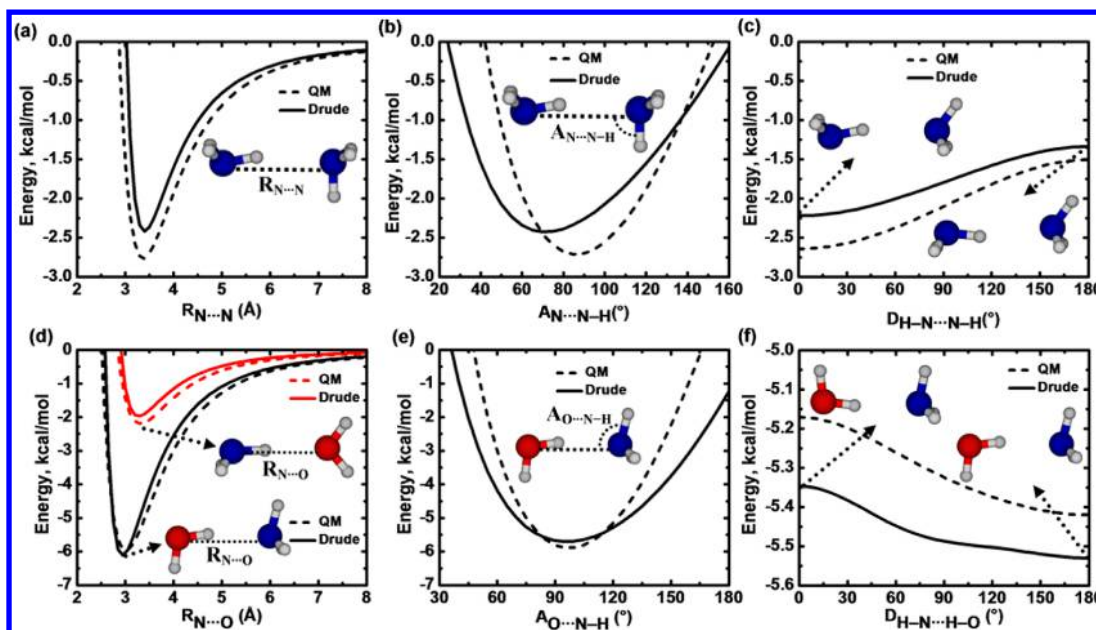


Figure 4. Potential energy curves for $\text{NH}_3\text{--NH}_3$ and $\text{NH}_3\text{--H}_2\text{O}$ complexes from ab initio MP2(FC)/6-311++G(d,p) calculations (dashed lines) and from polarizable models (solid lines). For the ammonia dimer, the following coordinates are scanned: (a) $\text{N}\cdots\text{N}$ distance in the eclipsed conformer; (b) $\text{N}\cdots\text{N}\cdots\text{H}$ angle at a $\text{N}\cdots\text{N}$ distance of 3.258 Å; (c) $\text{H}\cdots\text{N}\cdots\text{N}\cdots\text{H}$ dihedral at a $\text{N}\cdots\text{N}$ distance of 3.261 Å. For the ammonia–water dimer, the scanned curves are (d) $\text{N}\cdots\text{O}$ distance in the trans $\text{N}\cdots\text{H}\cdots\text{O}$ and the $\text{O}\cdots\text{H}\cdots\text{N}$ hydrogen-bonded isomers; (e) the $\text{O}\cdots\text{N}\cdots\text{H}$ angle at a $\text{N}\cdots\text{O}$ distance of 2.937 Å; (f) $\text{H}\cdots\text{N}\cdots\text{H}\cdots\text{O}$ dihedral at a $\text{N}\cdots\text{O}$ distance of 2.937 Å.

angle from 0 to 180° at 2.937 Å. While the conformer at 180° in curve 4f is the exact trans isomer, the one at 0° is a distorted cis structure, which results in a 0.25 kcal/mol energy difference between the two structures instead of the 0.01 kcal/mol expected for the fully relaxed structures (see Table 4).

3.3. Optimized Force Field. In previous work,⁸⁵ we have optimized a polarizable model for $\text{NH}_4^+\text{--H}_2\text{O}$ and $\text{NH}_4^+\text{--benzene}$ interactions based on the ab initio properties of the two complexes. Following this work, we now optimize a polarizable model for $\text{NH}_3\text{--NH}_3$ and $\text{NH}_3\text{--H}_2\text{O}$ interactions based on the ab initio properties of NH_3 and its dimers with NH_3 and H_2O . The equilibrium structural parameters for NH_3 (see section 2.2.1) are those from the MP2(FC)/6-311++G(d,p) optimized monomer: $b_0 = 1.0135$ Å and $\theta_0 = 107.29^\circ$. The corresponding force constants are chosen as $k_b = 525.0$ kcal/mol/Å² and $k_\theta = 84.0$ kcal/mol/rad² and result in the following vibrational frequencies for the gaseous monomer: ν_1 (N–H asymmetric stretching) = 3556 cm^{−1}, ν_2 (N–H wagging) = 1614 cm^{−1}, ν_3 (N–H symmetric stretching) = 3667 cm^{−1}, and ν_4 (H–N–H scissoring) = 2218 cm^{−1}. While the bond force constant is chosen to reproduce the MP2(FC)/6-311++G(d,p) bond-stretching frequencies (ν_1 and ν_3 , see Table 1), the angle force constant is set larger in order to avoid unphysical distortions of the NH_3 geometry during MD simulations. Although our ab initio calculations show that ammonia molecules retain their gas-phase monomeric structure in small clusters (with a maximum deviation of 0.011 Å for the NH bond length and of 1.5° for the NHN angle), the angle potential for ammonia was reported to be particularly important for the vapor-to-liquid equilibrium properties of ammonia.⁴⁹ For this reason, we use an ammonia model with rigid bonds but flexible angles.

The optimized nonbonded parameters are as follows: $q_{\text{H}} = 0.33192e$, $q_{\text{N}} = -0.99576e$, $\alpha_{\text{N}} = 1.6905$ Å³, $E_{\text{min,N}} = 0.1043429$ kcal/mol, $R_{\text{min,N}}/2 = 2.0780073$ Å, $E_{\text{min,H}} = 0.0699455$ kcal/

mol, and $R_{\text{min,H}}/2 = 0.5558178$ Å. The partial atomic charges reproduce the MP2-calculated dipole moment of gaseous NH_3 (1.782 D), and the isotropic Drude polarizability is set to the orientational average of the MP2-calculated molecular polarizability tensor. The LJ parameters for N and H are optimized to reproduce the binding energy and PESs of the $\text{NH}_3\text{--H}_2\text{O}$ dimer (see Table 4 and Figure 4). These parameters are used for all N–O, N–H, H–O, and H–H pairs (based on the Lorentz–Berthelot combination rules, eq 2), but separate LJ parameters are adjusted for N–N pairs, based on the ab initio properties of the ammonia dimer (see Table 3 and Figure 4): $E_{\text{min,NN}} = 0.1541785$ kcal/mol and $R_{\text{min,NN}}/2 = 2.0060673$ Å. Note that H atoms in the SWM4-NDP water model have no LJ parameters and therefore do not contribute to the LJ energy. In both cases, the parameters are first optimized based on the PESs of the dimers (calculated with rigid monomer geometries), then refined to reproduce their CP-corrected binding energies.⁸⁵ This later refinement results in a slight disagreement between the Drude and ab initio PESs (see Figure 4).

As seen from Table 3, the optimized model gives binding energies for the various ammonia clusters in good agreement with ab initio data and with previous potential models.^{29–32} It correctly reproduces the trend from the uncorrected energies E of dimer structures a, b, and c. The trend observed for the CP-corrected energies (E^{CP}) is likely due to overestimation of the BSSE of the stable dimer conformations. In comparison, the polarizable models of Janeiro-Barral et al.³¹ and Yu and Yang³² give binding energies in close agreement with E^{CP} for the dimer and trimer but tend to overestimate the energies of larger clusters. The optimized Drude model also reproduces the binding cooperativity in these clusters. For example, while the $\text{N}\cdots\text{N}$ separation in the eclipsed ammonia dimer is 3.366 Å, it is 3.340 Å in the trimer and 3.301 Å in the tetramer.

The NH_3 model displays good transferability when combined with the SWM4-NDP H_2O model,⁸³ as indicated

by the close agreement between E^{Drude} and E^{CP} energies for $\text{NH}_3(\text{H}_2\text{O})_n$ and $\text{H}_2\text{O}(\text{NH}_3)_n$ clusters (see Tables 4 and 5). The model also reproduces the binding cooperativity in $\text{NH}_3(\text{H}_2\text{O})_n$ (see Figure 2) and $\text{H}_2\text{O}(\text{NH}_3)_n$ clusters. For example, the Drude-optimized $\text{H}_2\text{O}(\text{NH}_3)_2$ complex shows separations between the heavy atoms in the $\text{O}\cdots\text{H}-\text{N}$, $\text{N}\cdots\text{H}-\text{N}$, and $\text{N}\cdots\text{H}-\text{O}$ hydrogen-bonded molecules that are 0.038, 0.051, and 0.023 Å shorter than the corresponding distances in the isolated dimers.

3.4. Liquid Ammonia. The Drude model for NH_3-NH_3 interaction is validated by calculating the structural, thermodynamic, and dynamic properties of liquid ammonia at its boiling point. For this purpose, a system of 250 ammonia molecules is simulated at the normal boiling point of liquid ammonia ($T = 239.8 \text{ K}$ and $p = 1 \text{ atm} = 0.1013 \text{ MPa}$). Four simulations with different initial configurations are run for 10 ns (40 ns total), and the liquid properties are calculated from the last 8 ns of each simulation. Under these thermodynamic conditions, the model yields an average molecular volume of 41.42 Å^3 and a density of $0.683 \pm 0.001 \text{ g/cm}^3$, in better agreement with the experimental value⁹⁴ (0.682 g/cm^3) than the values reported by Rizzo and Jorgensen³⁶ (0.697 g/cm^3), Honda⁴¹ (0.690 g/cm^3 at 277 K), Ren et al.⁵¹ (0.676 g/cm^3), and Eckl et al.⁴⁴ (0.686 g/cm^3 at 240 K and 0.1196 MPa).

Enthalpy of vaporization, ΔH_{vap} , is calculated from the average net gain of potential energy $\langle \Delta u \rangle$ upon formation of the dense system.⁹⁵

$$\begin{aligned}\Delta H_{\text{vap}} &= RT - \langle \Delta u \rangle \\ &= RT - (\langle u \rangle_l - \langle u \rangle_g) \\ &= RT - \left(\langle u \rangle_l - \frac{3}{2} RT \right)\end{aligned}\quad (7)$$

where R is the gas constant, T is the temperature, $\langle u \rangle_l$ is the average potential energy per mole in the liquid phase, and $\langle u \rangle_g$ is the average potential energy of gaseous NH_3 . For an NH_3 model with fixed NH bond lengths, only the angle-bending modes contribute to the gas-phase potential energy:

$$\langle u \rangle_g = \frac{3}{2} RT \quad (8)$$

The average potential energy of the simulated system is found to be $\langle u \rangle_l = -4.714 \text{ kcal/mol}$, which corresponds to $\Delta H_{\text{vap}} = 5.90 \pm 0.005 \text{ kcal/mol}$, in good agreement with the experimental value, 5.58 kcal/mol .⁹⁴ Again, it should be emphasized that the model was not adjusted for any of the bulk properties. By comparison, the AMOEBA force field of Ren et al.,⁵¹ calibrated specifically to reproduce both the density and the enthalpy of vaporization, yields $\Delta H_{\text{vap}} = 5.54 \text{ kcal/mol}$.

The self-diffusion coefficient of an ammonia molecule in the liquid state is obtained from the long-time limit of the mean-square displacement of the nitrogen atoms:⁹⁵

$$D_{\text{PBC}} = \lim_{t \rightarrow \infty} \frac{1}{6t} \left\langle \frac{1}{N} \sum_{i=1}^N [\mathbf{r}_{\text{N},i}(t) - \mathbf{r}_{\text{N},i}(0)]^2 \right\rangle \quad (9)$$

The resulting diffusion coefficient, obtained from a least-squares linear fit of the last 8 ns of the trajectories, is corrected for system-size dependence using the formula of Yeh and Hummer:⁹⁶

$$D = D_{\text{PBC}} + \frac{2.837297 k_{\text{B}} T}{6\pi\eta L} \quad (10)$$

where k_{B} is Boltzmann constant, η the shear viscosity of the solvent, and L is the average length of the cubic simulation box.⁹⁶ Using a value of 0.254 cP for the shear viscosity,¹ the self-diffusion coefficient of the bulk liquid is $D = 5.90 \pm 0.02 \times 10^{-9} \text{ m}^2 \text{ s}^{-1}$, in close agreement with the experimental value of $5.6 \times 10^{-9} \text{ m}^2 \text{ s}^{-1}$ reported by Garroway and Cotts¹⁴ and in excellent agreement with the experimental value of $5.83 \times 10^{-9} \text{ m}^2 \text{ s}^{-1}$ reported by O'Reilly et al.¹⁵ Compared to our calculated value, Impey and Klein reported a D_{PBC} value of $5.0 \times 10^{-9} \text{ m}^2 \text{ s}^{-1}$ (at $T = 260 \text{ K}$), which would correspond to a size-corrected D value of $6.6 \times 10^{-9} \text{ m}^2 \text{ s}^{-1}$.³³ Using two different potential models, Sagarik et al.²⁸ reported D_{PBC} values of $4.2 \times 10^{-9} \text{ m}^2 \text{ s}^{-1}$ and $4.4 \times 10^{-9} \text{ m}^2 \text{ s}^{-1}$ (at $T = 237 \text{ K}$) which would correspond to size-corrected D values of $5.28 \times 10^{-9} \text{ m}^2 \text{ s}^{-1}$ and $5.48 \times 10^{-9} \text{ m}^2 \text{ s}^{-1}$.

Isothermal compressibility measures the relative volume change accompanying any change in pressure:

$$\beta_T = -\frac{1}{V} \left(\frac{\partial V}{\partial p} \right)_T \quad (11)$$

The isothermal compressibility of a system of N particles in equilibrium at constant temperature and pressure is directly related to the volume fluctuations around its average value:⁹⁷

$$\beta_T = \frac{1}{k_{\text{B}} T} \frac{\langle \Delta V^2 \rangle_{NpT}}{\langle V \rangle_{NpT}} \quad (12)$$

where $\langle V \rangle_{NpT}$ is the average volume and $\langle \Delta V^2 \rangle_{NpT}$ are the average volume fluctuations. The isothermal compressibility of liquid ammonia at its boiling point (239.8 K) calculated using the Drude model is $0.74 \pm 0.05 \text{ GPa}^{-1}$, in excellent agreement with the experimental value of 0.74 GPa^{-1} at 238.0 K .⁹⁸

The dielectric constant of the liquid, ϵ , was calculated following the procedure reported for the SWM4-NDP water model.⁹⁵ The model shows a value of 122, which is overestimated compared to the experimental value of 22.6 at 238.15 K .¹⁷ This overestimation may be attributed to the higher dipole moment obtained from MP2 calculations of gaseous ammonia compared to the experimental value (see Table 1).

The molar heat capacity at constant pressure, C_p , is calculated from five simulations at different temperatures ($219.8, 224.8, 229.8, 234.8$, and 239.8 K) and at a constant pressure of 0.1013 MPa . The total energy U_{tot} and the volume V are averaged over time, and C_p at 239.8 K is calculated from a linear fit of $\langle U_{\text{tot}} \rangle + pV$ versus T .⁹⁷

$$C_p = \frac{1}{N} \left(\frac{\partial (\langle U_{\text{tot}} \rangle + p \langle V \rangle)}{\partial T} \right)_{T=239.8 \text{ K}, p=0.1013 \text{ MPa}} \quad (13)$$

The model shows a value of $C_p = 19.6 \text{ cal mol}^{-1} \text{ K}^{-1}$, in good agreement with the experimental value of $18.12 \text{ cal mol}^{-1} \text{ K}^{-1}$.¹³

Ricci et al.¹⁰ conducted neutron diffraction experiments with isotropic H/D substitution (NDIS) to investigate the microscopic structure of liquid ammonia at two sets of temperatures and pressures, one at $T = 213 \text{ K}$ and $p = 0.121 \text{ MPa}$ and the other at $T = 273 \text{ K}$ and $p = 0.483 \text{ MPa}$. A similar experiment was performed by Thompson et al.¹¹ to investigate the structure of ammonia and metallic lithium-ammonia solutions

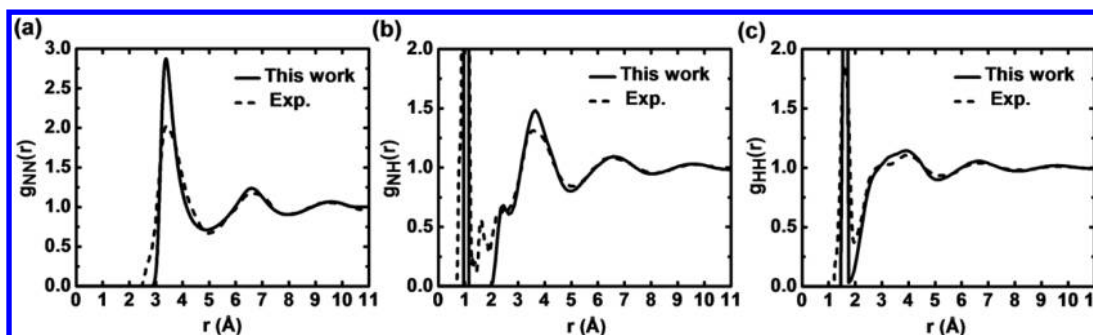


Figure 5. Radial distribution functions of ammonia at $T = 213.0$ K and $p = 0.121$ MPa calculated from MD simulation using the Drude model (solid lines) in comparison with NDIS experiment¹⁰ under the same conditions (dashed lines).

at 230 K. To compare with the Ricci et al. experiment, a system of 250 ammonia molecules is simulated for 10 ns at $T = 213$ K and $p = 0.121$ MPa. The structure of the liquid is analyzed from the $g_{NN}(r)$, $g_{NH}(r)$, and $g_{HH}(r)$ radial distribution functions (RDFs), shown in Figure 5. The agreement between the calculated and experimental RDFs is very good, especially given the fact that no adjustments were made to reproduce the liquid structure data.

The $g_{NN}(r)$ function (Figure 5a) shows three peaks centered at 3.37, 6.6, and 9.6 Å, indicating three well-defined solvation shells. The narrow shape of the first peak in the calculated $g_{NN}(r)$ is likely due to the steepness of the Lennard-Jones repulsive potential.⁹⁵ The coordination number (up to the first minimum in the $g_{NN}(r)$ curve, at 4.91 Å) is 12.5, in agreement with the experimental values of ~ 14 ammonia molecules reported by Ricci et al.¹⁰ and of ~ 12 reported by Thompson et al.¹¹

The $g_{NH}(r)$ function (Figure 5b) is similarly characterized by three peaks, located at 3.64, 6.6, and 9.6 Å. The high and narrow peak at $r \sim 1.0$ Å corresponds to the intramolecular NH bonds. The density at $r \sim 1.6$ Å in the experimental curve of Figure 5b corresponds to a residual signal from intramolecular HH pairs.¹⁰ Integration of $g_{NH}(r)$ over the range $1.9 \text{ Å} \leq r \leq 4.91 \text{ Å}$ shows 37.5 neighboring H atoms around a central nitrogen, consistent with the NN coordination number at the same distance range ($37.5 \div 3 = 12.5$). The shoulder at $r \sim 2.44$ Å matches the experimental shoulder observed at ~ 2.25 Å by Ricci et al.¹⁰ and at ~ 2.4 Å by Thompson et al.¹¹ and represents N \cdots H pairs directly involved in hydrogen bonds.¹⁰ The number of hydrogen bonds formed between a central nitrogen atom and its nearest neighbors can be estimated by integrating the function from 2.0 Å to the shallow minimum observed at 2.67 Å, which yields 2.0 hydrogen bonds per nitrogen atom, in agreement with the experimental numbers reported by Ricci et al.¹⁰ (less than 2) and by Thompson et al.¹¹ (2.1 ± 0.5).

The $g_{HH}(r)$ function (Figure 5c) has the same characteristic features as the experimental function. The peak at $r \sim 1.6$ Å corresponds to the intramolecular HH pairs. Although the calculated function does not display a distinct peak at ~ 2.7 Å, its broad profile and the very weak shoulder at almost the same position is consistent with experimental results. This shoulder corresponds to the shortest intermolecular HH separation in the hydrogen-bonded dimers.¹⁰

Since the number of first-shell molecules is much larger in liquid ammonia (12.5) than in liquid water (4.63),⁹⁵ the fraction of molecules forming a hydrogen bond with a central molecule is much smaller in ammonia than in water.

Although the model overestimates the dielectric constant and is slightly overestimating the vaporization enthalpy of fluid ammonia (by 6%), it yields density, diffusion coefficient, isothermal compressibility, heat capacity, and structure in very good agreement with the experimental results. We have therefore not reoptimized the model for better agreement in the calculated enthalpy of vaporization since this deteriorates the performance on the other properties. It will be shown in the following section that the discrepancy in ΔH_{vap} is approximately uniform over a wide range of pressures and therefore can be easily corrected.

3.5. Ammonia at Various p and T . The transferability of the NH_3 model is further tested by calculating the densities, vaporization enthalpies, diffusion coefficients, and structure of fluid ammonia under different thermodynamic conditions and comparing the results to available experimental data. See Figure 6 for an overview of the pressure and temperature conditions simulated in this work.

3.5.1. Density and Vaporization Enthalpy. The ammonia model is used in a total of 99 simulations: along the liquid–vapor phase boundary, and in the liquid and supercritical phases of fluid ammonia (under the thermodynamic conditions shown in blue and red in Figure 6). Each of the 99 systems is composed of 250 ammonia molecules and is simulated for 2×10 ns.

Figure 7a shows the calculated versus experimental⁹⁹ densities (see also Tables S1 and S2). The simulations show an average unsigned error of 3.6% for densities of simulations at $p \geq p_c$ (red circles on Figure 6; density values reported in Table S1) and of 1.5% for densities at the liquid–vapor boundary (blue triangles on Figure 6; density values reported in Table S2). The average overall unsigned error for all 99 simulations is 3.2%.

Figure 7b shows the calculated vaporization enthalpies from simulations at the liquid–vapor phase boundary versus the available corresponding experimental values¹⁰⁰ (see also Table S2). (No experimental data are available for ΔH_{vap} under the conditions shown in red in Figure 6, but calculated values are reported in Table S1.) Although the model systematically overestimates ΔH_{vap} (see Figure 7b and Table S2), the deviation from experimental data is approximately uniform over a wide range of temperatures and pressures and never more than 7.6%. On the basis of Figure 7b, we derive a correction for the calculated ΔH_{vap} as

$$\Delta H_{\text{vap}}^{\text{expt}} = 0.971 \times \Delta H_{\text{vap}}^{\text{calc}} - 0.154 \text{ kcal/mol} \quad (14)$$

This correction reduces the average unsigned error to one tenth of its uncorrected value (0.6% instead of 6.2%).

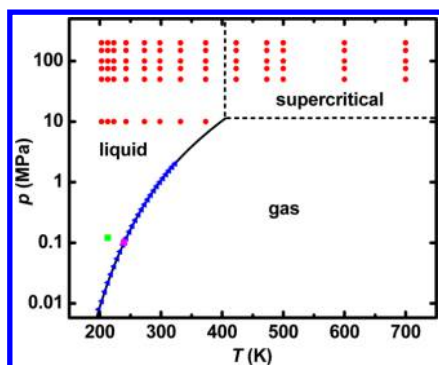


Figure 6. Phase diagram of NH_3 . The solid and dashed lines are phase boundaries, and their intersection is the critical point ($T_c = 405.55 \text{ K}$, $p_c = 11.38 \text{ MPa}$).¹ Red circles are the conditions at which densities, vaporization enthalpies, and self-diffusion coefficients are investigated (see Tables S1 and S3 of Supporting Information (SI)). Blue triangles are the pressure and temperature conditions at which densities and vaporization enthalpies are investigated (see Table S2 of SI). The pink square represents the normal boiling point of NH_3 ($T = 239.8 \text{ K}$, $p = 1 \text{ atm} = 0.1013 \text{ MPa}$),¹ and the green square represents one of Ricci et al.'s NDIS experimental conditions¹⁰ ($T = 213 \text{ K}$, $p = 0.121 \text{ MPa}$), at which the liquid structure of ammonia is investigated.

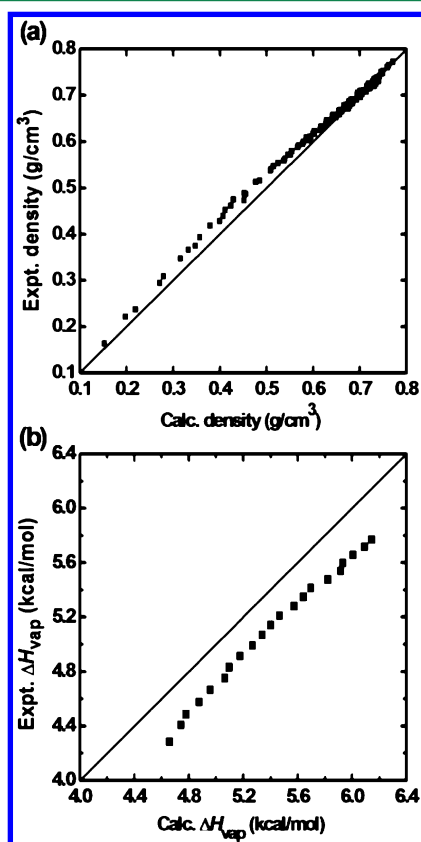


Figure 7. (a) Calculated versus experimental⁹⁹ densities of fluid ammonia under the thermodynamic conditions shown in red and blue in Figure 6 (also reported in Tables S1 and S2). (b) Calculated versus experimental¹⁰⁰ enthalpy of vaporization under the thermodynamic conditions shown in blue in Figure 6 (see also Table S2).

Since the NH_3 model reproduces the experimental densities of liquid and supercritical ammonia within an average error of 3.2% over a wide range of temperatures and pressures, it is expected to reliably describe the influence of temperature and pressure on the microscopic structure of the fluid.

We report in Figure 8 the $g_{\text{NN}}(r)$, $g_{\text{NH}}(r)$, and $g_{\text{HH}}(r)$ functions calculated at 50 MPa and at six different temperatures: 213, 273, 332, 423, 500, and 600 K. While the three functions display three intermolecular peaks (in addition to a shoulder in the $g_{\text{NH}}(r)$ function), only the first peak persists at high temperatures. The shoulders in the $g_{\text{NH}}(r)$ and $g_{\text{HH}}(r)$ functions at $\sim 2.4 \text{ \AA}$ and $\sim 2.7 \text{ \AA}$, respectively, which indicate hydrogen bonding between ammonia molecules, decrease with increasing temperature. This indicates that preferential orientation of ammonia molecules—which allows for hydrogen bonding—decreases at high temperature.

Previous theoretical investigations have shown that while temperature strongly determines the local structure of liquid and supercritical ammonia, the influence of pressure is almost negligible.^{45,47} Pressure and temperature-induced structural changes are analyzed by calculating the coordination number of the ammonia fluid at selected temperatures and pressures (see Table S4). The simulations show that the average coordination number decreases as the temperature increases, and that the decreasing trend is more pronounced at low pressure.⁴⁷ While the pressure effect is minimal at low temperatures, it has a significant influence on the local structure at high temperatures. For example, a rise in pressure from 50 to 200 MPa increases the N–N coordination number by 0.4 at 203 K but by 5.3 at 700 K.

3.5.2. Self-Diffusion Coefficient. Diffusion coefficients at high pressure have several applications in the chemical industry.⁴⁷ While diffusion data can be obtained from nuclear magnetic resonance and isotope trace techniques, experiments are difficult and time-consuming.^{16,47} Provided they are reliable, predictions from molecular dynamics simulations are therefore a valuable complement to experimental data.

Groß et al.¹⁶ have measured the self-diffusion coefficients for fluid ammonia using the NMR pulsed field gradient method at temperatures up to 473 K and pressures up to 200 MPa. To test the performance of the optimized ammonia model, MD simulations are performed at the different temperatures and pressures considered experimentally.¹⁶ We also extend the investigation to higher temperatures, up to 700 K. A total of 73 thermodynamic conditions are simulated (see Figure 6 and Table S3 of SI). Each simulation is performed for a system of 2000 ammonia molecules for 8 ns in the *NPT* ensemble, and the self-diffusion coefficient is calculated from the last 6 ns using eq 9. Such a large simulation system is necessary to prevent finite-size effects from speeding up the diffusion of large molecular clusters in the low-density supercritical phase and from causing an artificial non-Arrhenius behavior for the diffusivity. Whenever possible, the calculated self-diffusion coefficients are corrected for system-size dependence using eq 10,⁹⁶ with the shear viscosities of the fluid obtained from ref 99. The calculated self-diffusion coefficients are plotted against the experimental data in Figure 9.

Figure 9 (and Table S3 of SI) shows very good agreement between the calculated and experimentally measured self-diffusion coefficients. Excluding the experimental point at 373 K and 10 MPa, which is significantly outside the Arrhenius trend, and is likely an aberration, the average unsigned error on the calculated D is 3.3%. This error is lower than the average error of 6.0% reported by Feng et al.,⁴⁷ which are calculated without the correction of eq 10. (With the correction of eq 10, the average unsigned error on Feng et al.'s results increases to 18%.) It should also be noted that the self-diffusion coefficients reported by Feng et al. at temperatures higher than 332 K are

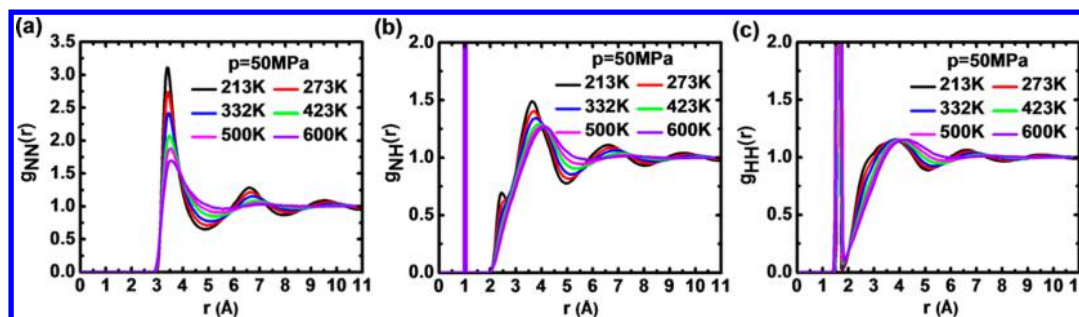


Figure 8. Temperature dependence of the (a) nitrogen–nitrogen, (b) nitrogen–hydrogen, and (c) hydrogen–hydrogen radial distribution functions in fluid NH_3 at $p = 50$ MPa.

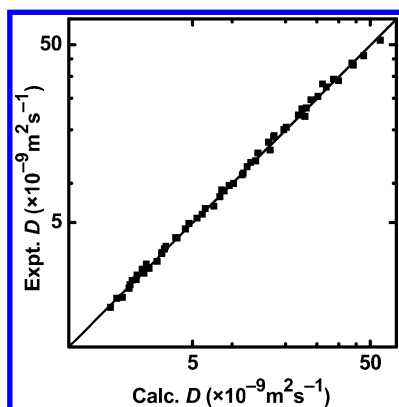


Figure 9. Log–log plot of the calculated versus experimental¹⁶ self-diffusion coefficients of ammonia at some of the thermodynamic conditions shown in red in Figure 6 (see also Table S3 of SI).

based on *NVT* simulations using the experimental density rather than the density obtained from their model.^{47,101} As in previous experimental¹⁶ and theoretical^{47,102} investigations, the data show a non-Arrhenius relation between $\ln D$ and $1/T$ at high temperatures and low pressures (see Table S3).

3.6. Hydration of NH_3 . As reported in sections 3.1.3 and 3.1.4, the NH_3 model (in combination with the SWM4-NDP water model⁸³) reproduces the binding energies and structural properties of the $\text{NH}_3(\text{H}_2\text{O})_n$ and $\text{H}_2\text{O}(\text{NH}_3)_n$ ($n = 2-4$) clusters. As a further test of transferability, the free energy of hydration of H_2O relative to that of NH_3 in bulk water, $\Delta\Delta G_{\text{hydr}}(\text{NH}_3 \rightarrow \text{H}_2\text{O})$, is calculated at $T = 298.15$ K and $p = 0.1013$ MPa. The calculations show a value of -2.0 ± 0.1 kcal/mol. Taking into account the hydration free energy of the SWM4-NDP water molecule, -5.9 ± 0.1 kcal/mol,⁸³ this results in a hydration free energy of NH_3 equal to -3.9 ± 0.1 kcal/mol, in good agreement with the experimental value of -4.3 kcal/mol^{103,104} and with hybrid QM/MM MD simulation results (-4.5 ± 0.2 kcal/mol).⁷⁶ By comparison, Rizzo and Jorgensen³⁶ have reported a value of -3.34 kcal/mol using a pairwise-additive model. Dang and Garrett⁷³ have reported a value of -5.6 ± 0.5 kcal/mol using a polarizable model, and Pártay et al.⁷⁵ have reported a value of -1.9 kcal/mol.

The hydration structure of NH_3 is investigated from the simulation of one ammonia molecule in 249 water molecules at 298.15 K and 0.1013 MPa. The $g_{\text{NO}}(r)$, $g_{\text{NH}}(r)$, $g_{\text{HO}}(r)$, and $g_{\text{HH}}(r)$ RDFs between the ammonia solute and its water solvent are reported in Figure 10. The $g_{\text{NH}}(r)$ RDF exhibits a narrow and well-separated peak at 1.93 Å that corresponds to $\text{N}\cdots\text{H}-\text{O}$ hydrogen-bonded pairs. Integration up to the minimum at 2.55 Å yields a coordination number of 1.8, indicating that the N

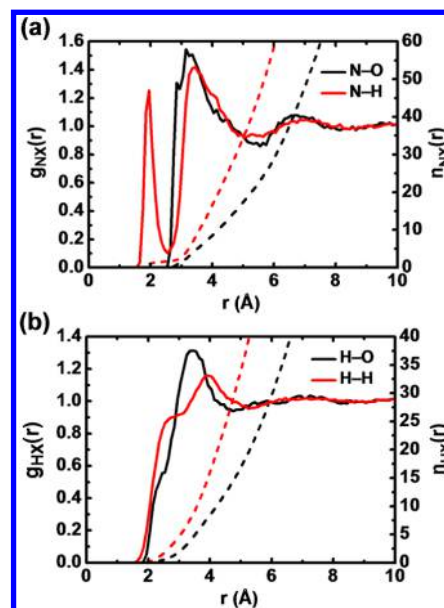


Figure 10. Radial distribution functions, $g(r)$, between a single ammonia molecule solvated by 249 water molecules at $T = 298.15$ K and $p = 1$ atm = 0.1013 MPa. Panel a shows nitrogen–oxygen (black) and nitrogen–hydrogen (red) RDFs, and panel b shows hydrogen–oxygen (black) and hydrogen–hydrogen (red) RDFs. Dashed lines represent the corresponding running coordination numbers, $n(r)$.

atom acts as a hydrogen bond acceptor to about two water molecules. In comparison, Rizzo and Jorgensen³⁶ have calculated 1.23 $\text{N}\cdots\text{H}-\text{O}$ hydrogen bonds per N atom. A second peak centered at 3.43 Å depicts a more flexible solvation structure, as evidenced by the broader and less symmetric peak. Integration up to the second minimum (at 5.5 Å) results in a coordination number of ~ 46 hydrogen atoms, indicating ~ 23 water molecules in the first solvation shell of NH_3 . The $g_{\text{NO}}(r)$ RDF exhibits a shoulder at 2.88 Å due to $\text{N}\cdots\text{H}-\text{O}$ hydrogen bonds, followed by a peak at 3.17 Å due to $\text{N}-\text{H}\cdots\text{O}$ bonds (see Figure 2). Integration up to the minimum at 5.53 Å confirms that the first solvation shell of NH_3 contains ~ 23 water molecules.

The RDFs are consistent with a picture of NH_3 hydration in which approximately two (1.8 on average) water molecules are forming strong $\text{N}\cdots\text{H}-\text{O}$ hydrogen bonds on the acceptor side of the ammonia molecule, while the donor side of the molecule is interacting with a large number (~ 21) of water molecules forming transient $\text{N}-\text{H}\cdots\text{O}$ hydrogen bonds.

3.7. Water Solvated in Ammonia. The $g_{\text{ON}}(r)$, $g_{\text{OH}}(r)$, $g_{\text{HN}}(r)$, and $g_{\text{HH}}(r)$ RDFs obtained from the simulation of one

water molecule in 249 ammonia molecules at 239.8 K and 0.1013 MPa are reported in Figure 11. The $g_{\text{ON}}(r)$ RDF

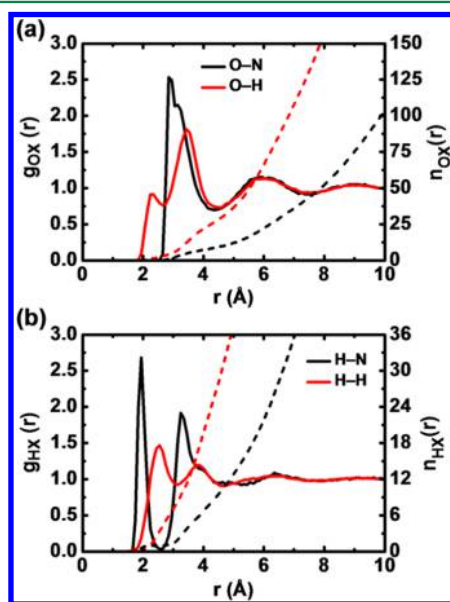


Figure 11. Radial distribution functions, $g(r)$, between a single water molecule solvated by 249 ammonia molecules at $T = 239.8$ K and $p = 1$ atm = 0.1013 MPa. Panel a shows oxygen–nitrogen (black) and oxygen–hydrogen (red) RDFs, and panel b shows hydrogen–nitrogen (black) and hydrogen–hydrogen (red) RDFs. Dashed lines represent the corresponding running coordination numbers, $n(r)$.

(Figure 11a) exhibits a peak with a maximum at 2.88 Å due to O–H···N hydrogen-bonded pairs and a shoulder at 3.17 Å due to O···H–N pairs. Integration up to the minimum at 4.48 Å shows 9.1 ammonia molecules in the first solvation shell of water. The $g_{\text{OH}}(r)$ RDF exhibits a peak at 2.31 Å (due to O···H–N pairs) that overlaps with a peak at 3.46 Å. Integration of $g_{\text{OH}}(r)$ up to the minimum at 2.67 Å shows 3.0 ammonia hydrogen atoms at a coordinating distance from the water oxygen. Integration from 2.67 Å to 4.48 Å shows further 24.4 ammonia hydrogen atoms. The total number of ammonia hydrogens around the water molecule up to the first solvation shell, $3.0 + 24.4 = 27.4$, is consistent with 9.1 ammonia molecules around water.

The $g_{\text{HN}}(r)$ RDF (Figure 11b) displays a narrow and well-separated first peak with a maximum at 1.95 Å, due to N···H–O hydrogen bonding. Integration up to the minimum at 2.60 Å results in a coordination number of 1.0, indicating that water is forming a total of two N···H–O hydrogen bonds with ammonia molecules in its first solvation shell. The $g_{\text{HH}}(r)$ RDF shows two peaks at 2.55 Å and 3.85 Å with their minima at 3.14 Å and ~4.7 Å, respectively.

To summarize, the first solvation shell of the water molecule is composed of approximately nine ammonia molecules, including two acting as H-bond acceptors. The remaining seven ammonia molecules act as transient H-bond donors, three at a time.

3.8. Water–Ammonia Mixtures. We calculate the density and structure of various aqueous ammonia mixtures under different thermodynamic conditions: at $T = 239.8$, 273.15, and 293.15 K and at p corresponding to the vapor pressure of pure ammonia at the temperature simulated (0.1013, 0.4294, and 0.8571 MPa, respectively). The mixtures are composed of a total of 250 molecules with the ammonia molar fraction, x_{NH_3} ,

going from 0 to 100%. Two 10-ns simulations are performed for each system under each set of thermodynamic conditions. The water-rich systems at $T = 239.8$ K are simulated in the supercooled state. Figure 12 presents the calculated densities as

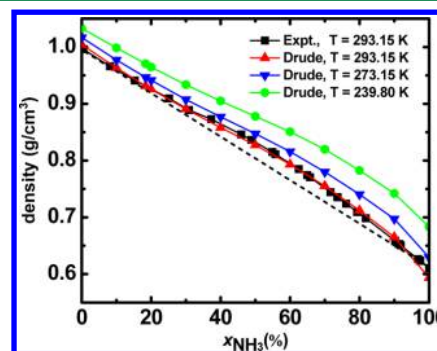


Figure 12. Densities of water–ammonia mixtures calculated using the Drude model at 239.8 K (green), 273.15 K (blue), and 293.15 K (red) and measured experimentally¹⁰⁵ at 293.15 K (black). The straight, dashed black line connects the experimental densities at $x_{\text{NH}_3} = 0$ and 100%.

a function of the composition (see also Table S5), together with the experimental densities measured by King et al.¹⁰⁵ at 293.15 K. The calculated densities are in excellent agreement with experimental results, with a maximum error of 1.7%. Figure 12 shows a nonlinear trend in the density–composition plot, with significant deviation from ideality for $x_{\text{NH}_3} > 20$ –30%.

We plot in Figure 13 the total pair distribution function $g_{(\text{N}+\text{O})-(\text{N}+\text{O})}(r)$ for some of the compositions simulated at

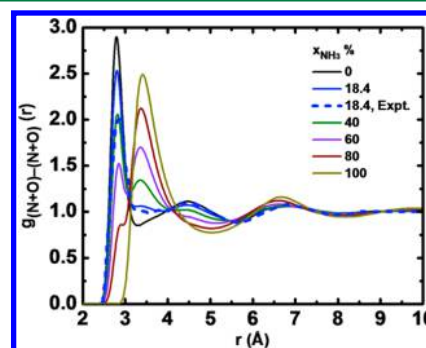


Figure 13. Total pair distribution function for aqueous ammonia solutions at different ammonia concentrations calculated from simulations at 273.15 K and 0.4294 MPa. The experimental⁸ X-ray function for $x_{\text{NH}_3} = 18.4\%$ at 277.15 K is shown as a dashed line.

273.15 K, along with the experimental function reported by Narten⁸ for $x_{\text{NH}_3} = 18.4\%$ at 277.15 K. The figure shows that, as x_{NH_3} increases, the intensity of the band centered at ~2.8 Å decreases while the intensity of the band centered at ~3.4 Å increases. In comparison, the experimental $g_{(\text{N}+\text{O})-(\text{N}+\text{O})}(r)$ RDF displays a first maximum that shifts from 2.82 Å for water to 3.4 Å for ammonia.⁸ The first peak corresponds to hydrogen-bonded O···O and N···O pairs. Its position is almost unaffected by x_{NH_3} (2.79 Å in pure water and only 2.85 Å at $x_{\text{NH}_3} = 80\%$) because the water–water and ammonia–water dimers have comparable molecular separations (see section 3.1.3). The second peak, at ~3.4 Å, is due to N···N pairs. The pair

distribution function calculated for $x_{\text{NH}_3} = 18.4\%$ follows the experimental distribution very closely. The only significant difference is the higher intensity of the calculated first peak, which (again) is likely the result of the steepness of the Lennard-Jones repulsive potential,⁹⁵ in addition to the packing of molecules being slightly closer at 273.15 K than at 277.15 K (the experimental temperature).

The weak intensity of the peak at ~ 3.4 Å at low ammonia concentrations (see Figure 13) confirms the absence of ammonia aggregation, in agreement with the experimental X-ray diffraction results.⁸ The results also agree with previous theoretical investigations.⁶⁹ Tanabe and Rode have simulated the structure of an 18.45% aqueous ammonia solution at 293.15 K and 0.1013 MPa and found that hydrogen bonding between ammonia molecules is hardly present at this concentration.⁶⁹

In order to understand the microscopic structure giving rise to the observed nonideal mixing properties, we plot in Figure 14 the numbers of H-bonds formed between ammonia and

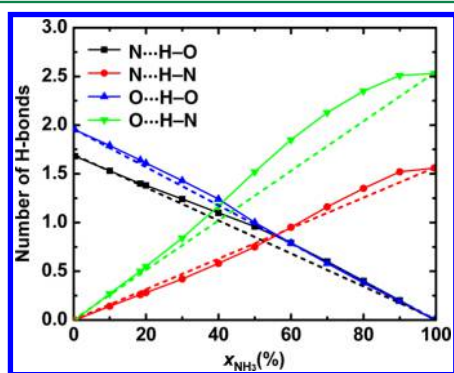


Figure 14. Number of hydrogen bonds per ammonia molecule due to $\text{N}\cdots\text{H}-\text{O}$ and $\text{N}\cdots\text{H}-\text{N}$ interactions, and per water molecule due to $\text{O}\cdots\text{H}-\text{O}$ and $\text{O}\cdots\text{H}-\text{N}$ interactions, as a function of ammonia molar fraction. Numbers are calculated by integrating the corresponding RDFs (see text). The highest coordination numbers in the black and green curves are calculated from the simulation of one ammonia molecule in 249 water molecules and of one water molecule in 249 ammonia molecules, respectively (at $T = 273.15$ K and $p = 0.4294$ MPa).

water molecules due to $\text{N}\cdots\text{H}-\text{O}$, $\text{N}\cdots\text{H}-\text{N}$, $\text{O}\cdots\text{H}-\text{O}$, and $\text{O}\cdots\text{H}-\text{N}$ interactions, as a function of the ammonia mole fraction at 273.15 K and 0.4294 MPa (see also Table S6). These are calculated by integrating functions $g_{\text{N}-\text{H}(\text{H}_2\text{O})}(r)$, $g_{\text{N}-\text{H}(\text{NH}_3)}(r)$, $g_{\text{O}-\text{H}(\text{H}_2\text{O})}(r)$, and $g_{\text{O}-\text{H}(\text{NH}_3)}(r)$ up to $r = 2.55$, 2.67, 2.45, and 2.67 Å, respectively. These distances represent the minimum of the first intermolecular peak of each function and are almost composition-independent. The dashed lines in Figure 14 represent the trends expected for ideal mixing. The plot shows large deviations from ideal mixing in the numbers of $\text{N}\cdots\text{H}-\text{O}$ and $\text{O}\cdots\text{H}-\text{N}$ hydrogen bonds for $x_{\text{NH}_3} > 20\text{--}30\%$. On the other hand, it shows smaller deviations in the numbers of $\text{O}\cdots\text{H}-\text{O}$ and $\text{N}\cdots\text{H}-\text{N}$ hydrogen bonds: water–water pairs are slightly enriched for $x_{\text{NH}_3} < 50\text{--}60\%$, and ammonia–ammonia pairs are slightly enriched for $x_{\text{NH}_3} > 50\text{--}60\%$. In other words, water–ammonia association is stronger in ammonia-rich mixtures than in water-rich mixtures. This is consistent with the fact that $\text{O}-\text{H}\cdots\text{N}$ hydrogen bonds are significantly stronger than $\text{N}-\text{H}\cdots\text{N}$ bonds but comparable to $\text{O}-\text{H}\cdots\text{O}$ bonds—at least in the gas phase. Using a more

stringent definition of hydrogen bonding, Paul and Chandra⁷⁴ find 1.3 hydrogen bonds per ammonia molecule in neat ammonia, compared to 1.56 from the present simulations.

The features observed in the density-composition plot (Figure 12) can thus be interpreted in terms of the local structure of the aqueous mixtures as follows: At low NH_3 concentrations ($x_{\text{NH}_3} < 20\text{--}30\%$), in the composition range where excess density ($\rho - \rho_{\text{ideal}}$) is negligible, ammonia molecules are dispersed in solution and ammonia–water interactions are nonspecific. However, at higher concentrations, ammonia–water pairs—particularly those forming $\text{O}-\text{H}\cdots\text{N}$ bonds, which are significantly more energetic and shorter than $\text{N}-\text{H}\cdots\text{N}$ bonds—become more pronounced and result in a positive excess density.

$\Delta G_{\text{solv}}(\text{H}_2\text{O})$, the solvation free energy of H_2O , and $\Delta G_{\text{solv}}(\text{NH}_3)$, the solvation free energy of NH_3 , are calculated at different mixture compositions and temperatures. The results, along with the free energy difference $\Delta\Delta G_{\text{solv}} = \Delta G_{\text{solv}}(\text{H}_2\text{O}) - \Delta G_{\text{solv}}(\text{NH}_3)$, are shown in Figure 15 (see also Table S7). Figure 15a shows $\Delta G_{\text{solv}}(\text{H}_2\text{O})$ to be approximately

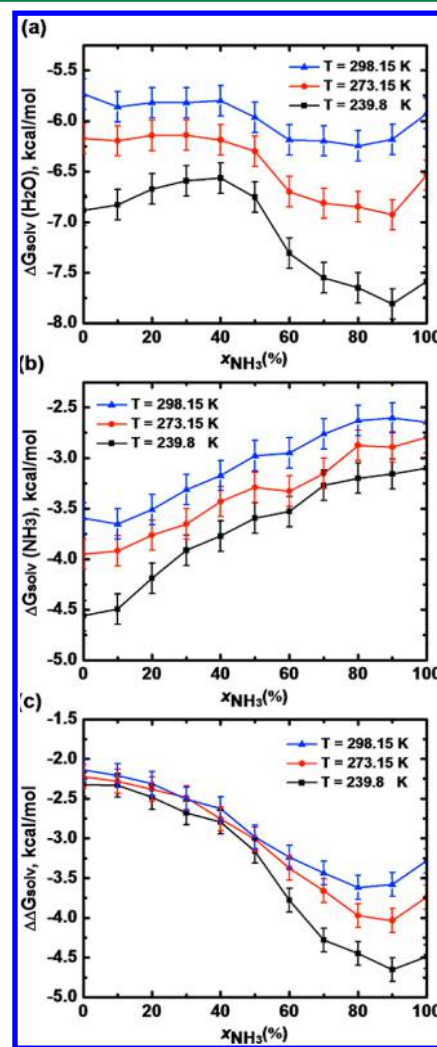


Figure 15. Solvation free energies of H_2O (a), NH_3 (b), and H_2O relative to NH_3 (c) as a function of temperature and ammonia molar fraction. Three thermodynamic conditions are studied: $T = 239.8$, 273.15, and 298.15 K (with $p = 0.1013$, 0.4294, and 1.0030 MPa, respectively). Error bars are typically equal to ± 0.15 kcal/mol.

constant for $x_{\text{NH}_3} < 50\%$ and to increase (in absolute value) at higher ammonia concentrations. While solvation free energy is not easily decomposable into contributions from the various components of the mixture, this trend is consistent with the fact that, for ammonia-rich mixtures, each water molecule is involved in an excess of O–H...N hydrogen bonds, which are stronger. The slight decrease in the solvation free energy in pure ammonia can likely be attributed to the complete absence of N...H–O bonds and their replacement by weaker N...H–N bonds. The solvation free energy decreases with temperature, with the influence of temperature being more pronounced at higher ammonia mole fractions.

The solvation free energy of ammonia (Figure 15b) decreases almost uniformly with ammonia concentration. This trend can probably be attributed to the gradual replacement of strong N...H–O bonds by weaker N...H–N bonds (see Figure 14, black and red curves).

The relative free energy, $\Delta\Delta G_{\text{solv}}$ (Figure 15c), shows a systematic preference for water that increases with ammonia concentration and is at a maximum for x_{NH_3} around 80–90%. The preference for water over ammonia becomes more temperature-dependent for $x_{\text{NH}_3} > \sim 50\%$, due mostly to the temperature-dependence of $\Delta G_{\text{solv}}(\text{H}_2\text{O})$.

4. CONCLUSION

Unlike the previously developed SWM4-NDP polarizable model for water,⁸³ which was adjusted explicitly to reproduce bulk properties of water, the present model for ammonia is adjusted solely based on ab initio properties of the NH_3 monomer and the NH_3 – NH_3 and NH_3 – H_2O dimers. The model reproduces the structure, density, self-diffusion coefficient, heat capacity, and compressibility of liquid ammonia, as well as the hydration free energy of NH_3 . It also reproduces experimental properties of liquid ammonia over a wide range of temperatures and pressures. As further indication of its transferability, it accurately reproduces the experimental structure and densities of aqueous ammonia solutions. While this strictly ab initio approach to force field parametrization has been reported to give results in agreement with ab initio and experimental data,^{85,106,107} it may not be generally applicable.

The model provides a powerful tool to investigate the properties of fluid ammonia under thermodynamic conditions for which experiments are difficult to perform. It has been used in combination with the SWM4-NDP water model to analyze the structure of aqueous ammonia mixtures and will be used in future work to simulate ion solvation in liquid and aqueous ammonia solutions and gain insight into the general phenomenon of preferential solvation.

■ ASSOCIATED CONTENT

Supporting Information

Seven tables including density, heat of vaporization, self-diffusion coefficient, coordination numbers of liquid ammonia under different thermodynamic conditions, density of aqueous ammonia, number of hydrogen bonds in aqueous ammonia, and solvation free energy of ammonia and water in aqueous ammonia. This information is available free of charge via the Internet at <http://pubs.acs.org>

■ AUTHOR INFORMATION

Corresponding Author

*Tel.: +1-514-848-2424, extension 5314. Fax: +1-514-848-2868. E-mail: guillaume.lamoureux@concordia.ca

Notes

The authors declare no competing financial interest.

†On leave from Department of Chemistry, Faculty of Science, Assiut University, Assiut 71516, Egypt

■ ACKNOWLEDGMENTS

We thank Maria Antonietta Ricci for providing the original data from ref 10. This work was supported in part by an FQRNT Nouveaux chercheurs grant and an NSERC Discovery grant to G.L. and by a PROTEO scholarship, a GEPROM scholarship, and a Power Corporation of Canada graduate fellowship to E.A.O. Computational resources were provided by Calcul Québec.

■ REFERENCES

- (1) Lagowski, J. J. *Synth. React. Inorg., Met.-Org., Nano-Metal Chem.* **2007**, *37*, 115–153.
- (2) Lagowski, J. J. *Pure Appl. Chem.* **1971**, *25*, 429–456.
- (3) Mifflin, B. J.; Lea, P. J. *Annu. Rev. Plant Physiol.* **1977**, *28*, 299–329.
- (4) Ninnemann, O.; Jauniaux, J.-C.; Frommer, W. B. *EMBO J.* **1994**, *13*, 3464–3471.
- (5) Marini, A.-M.; Urrestarazu, A.; Beauwens, R.; André, B. *Trends Biochem. Sci.* **1997**, *22*, 460–461.
- (6) Marini, A.-M.; Soussi-Boudekou, S.; Vissers, S.; André, B. *Mol. Cell. Biol.* **1997**, *17*, 4282–4293.
- (7) Marini, A.-M.; Vissers, S.; Urrestarazu, A.; André, B. *EMBO J.* **1994**, *13*, 3456–3463.
- (8) Narten, A. H. *J. Chem. Phys.* **1968**, *49*, 1692–1696.
- (9) Narten, A. H. *J. Chem. Phys.* **1977**, *66*, 3117–3120.
- (10) Ricci, M. A.; Nardone, M.; Ricci, F. P.; Andreani, C.; Soper, A. K. *J. Chem. Phys.* **1995**, *102*, 7650–7655.
- (11) Thompson, H.; Wasse, J. C.; Skipper, N. T.; Hayama, S.; Bowron, D. T.; Soper, A. K. *J. Am. Chem. Soc.* **2003**, *125*, 2572–2581.
- (12) Kasahara, K.; Munakata, T.; Uematsu, M. *J. Chem. Thermodyn.* **1999**, *31*, 1273–1281.
- (13) Overstreet, R.; Giaque, W. F. *J. Am. Chem. Soc.* **1937**, *59*, 254–259.
- (14) Garroway, A. N.; Cotts, R. M. *Phys. Rev. A* **1973**, *7*, 635–648.
- (15) O'Reilly, D. E.; Peterson, E. M.; Scheie, C. E. *J. Chem. Phys.* **1973**, *58*, 4072–4075.
- (16) Groß, T.; Buchhauser, J.; Price, W. E.; Tarassov, I. N.; H.-D. Lüdemann, H.-D. *J. Mol. Liq.* **1997**, *73–74*, 433–444.
- (17) Billaud, G.; Demortier, A. *J. Phys. Chem.* **1975**, *79*, 3053–3055.
- (18) Plank, C. J.; Herschel, H. *J. Am. Chem. Soc.* **1939**, *61*, 3590–3591.
- (19) Osborne, N. S.; Van Dusen, M. S. *J. Am. Chem. Soc.* **1918**, *40*, 14–25.
- (20) Howard, M. J.; Burdinski, S.; Giese, C. F.; Gentry, W. R. *J. Chem. Phys.* **1984**, *80*, 4137–4141.
- (21) Fraser, G. T.; Nelson, D. D.; Charo, A.; Klemperer, W. J. *J. Chem. Phys.* **1985**, *82*, 2535–2546.
- (22) Snels, M.; Fantoni, R.; Sanders, R.; Meerts, W. L. *J. Chem. Phys.* **1987**, *115*, 79–91.
- (23) Kamke, W.; Herrmann, R.; Wang, Z.; Hertel, I. V. *Z. Phys. D: At., Mol. Clusters* **1988**, *10*, 491–497.
- (24) Marshall, M. D.; Izgi, K. C.; Muenter, J. S. *J. Chem. Phys.* **1997**, *107*, 1037–1044.
- (25) Lee, J. S.; Park, S. Y. *J. Chem. Phys.* **2000**, *112*, 230–237.
- (26) Kulkarni, S. A.; Pathak, R. K. *J. Chem. Phys. Lett.* **2001**, *336*, 278–283.

- (27) Janeiro-Barral, P. E.; Mella, M. J. *Phys. Chem. A* **2006**, *110*, 11244–11251.
- (28) Sagarik, K. P.; Ahlrichs, R.; Brode, S. *Mol. Phys.* **1986**, *57*, 1247–1264.
- (29) Greer, J. C.; Ahlrichs, R.; Hertel, I. V. *Chem. Phys.* **1989**, *133*, 191–197.
- (30) Beu, T. A.; Buck, U. J. *Chem. Phys.* **2001**, *114*, 7848–7852.
- (31) Janeiro-Barral, P. E.; Mella, M.; Curotto, E. J. *Phys. Chem. A* **2008**, *112*, 2888–2898.
- (32) Yu, L.; Yang, Z.-Z. *J. Chem. Phys.* **2010**, *132*, 174109–1–174109–11.
- (33) Impey, R. W.; Klein, M. L. *Chem. Phys. Lett.* **1984**, *104*, 579–582.
- (34) Almeida, T. S.; Coutinho, K.; Cabral, B. J. C.; Canuto, S. J. *Chem. Phys.* **2008**, *128*, 014506–1–014506–9.
- (35) Hinchliffe, A.; Bounds, D. G.; Klein, M. L.; McDonald, I. R.; Righini, R. J. *Chem. Phys.* **1981**, *74*, 1211–1216.
- (36) Rizzo, R. C.; Jorgensen, W. L. *J. Am. Chem. Soc.* **1999**, *121*, 4827–4836.
- (37) Kristóf, T.; Vorholz, J.; Liszi, J.; Rumpf, B.; Maurer, G. *Mol. Phys.* **1999**, *97*, 1129–1137.
- (38) Diraison, M.; Martyna, G. J.; Tuckerman, M. E. *J. Chem. Phys.* **1999**, *111*, 1096–1103.
- (39) Kiselev, M.; Kerdcharoen, T.; Hannongbua, S.; Heinzinger, K. *Chem. Phys. Lett.* **2000**, *327*, 425–428.
- (40) Hannongbua, S. J. *Chem. Phys.* **2000**, *113*, 4707–4712.
- (41) Honda, K. *Bull. Chem. Soc. Jpn.* **2000**, *73*, 289–295.
- (42) Boese, A. D.; Chandra, A.; Martin, J. M. L.; Marx, D. *J. Chem. Phys.* **2003**, *119*, S965–S980.
- (43) Tongraar, A.; Kerdcharoen, T.; Hannongbua, S. J. *Phys. Chem. A* **2006**, *110*, 4924–4929.
- (44) Eckl, B.; Vrabec, J.; Hasse, H. *Mol. Phys.* **2008**, *106*, 1039–1046.
- (45) Chowdhuri, S.; Chakraborty, D.; Chandra, A. *Ind. J. Phys.* **2009**, *83*, 91–100.
- (46) Tassaing, T.; Soetens, J.-C.; Vyalov, I.; Kiselev, M.; Idrissi, A. J. *Chem. Phys.* **2010**, *133*, 214505–1–214505–8.
- (47) Feng, H.; Liu, X.; Gao, W.; Chen, X.; Wang, J.; Chen, L.; Lüdemann, H.-D. *Phys. Chem. Chem. Phys.* **2010**, *12*, 15007–15017.
- (48) Vyalov, I.; Kiselev, M.; Tassaing, T.; Soetens, J. C.; Idrissi, A. J. *Phys. Chem. B* **2010**, *114*, 15003–15010.
- (49) Engin, C.; Merker, T.; Vrabec, J.; Hasse, H. *Mol. Phys.* **2011**, *109*, 619–624.
- (50) Abbaspour, M. *Chem. Phys.* **2011**, *389*, 121–127.
- (51) Ren, P.; Wu, C.; Ponder, J. W. *J. Chem. Theory Comput.* **2011**, *7*, 3143–3161.
- (52) Tillner-Roth, R.; Friend, D. G. *J. Phys. Chem. Ref. Data* **1998**, *27*, 45–61.
- (53) Herbine, P.; Dyke, T. R. *J. Chem. Phys.* **1985**, *83*, 3768–3774.
- (54) Stockman, P. A.; Bumgarner, R. E.; Suzuki, S.; Blake, G. A. *J. Chem. Phys.* **1992**, *96*, 2496–2510.
- (55) Fraser, G. T.; Suenram, R. D. *J. Chem. Phys.* **1992**, *96*, 7287–7297.
- (56) Kuma, S.; Slipchenko, M. N.; Momose, T.; Vilesov, A. F. *Chem. Phys. Lett.* **2007**, *439*, 265–269.
- (57) Mollner, A. K.; Casterline, B. E.; Ch'ng, L. C.; Reisler, H. *J. Phys. Chem. A* **2009**, *113*, 10174–10183.
- (58) Tuma, C.; Boese, A. D.; Handy, N. C. *Phys. Chem. Chem. Phys.* **1999**, *1*, 3939–3947.
- (59) Sadlej, J.; Moszynski, R.; Dobrowolski, J. Cz.; Mazurek, A. P. *J. Phys. Chem. A* **1999**, *103*, 8528–8536.
- (60) Rappé, A. K.; Bernstein, E. R. *J. Phys. Chem. A* **2000**, *104*, 6117–6128.
- (61) Rzepkowska, J.; Uras, N.; Sadlej, J.; Buch, V. *J. Phys. Chem. A* **2002**, *106*, 1790–1796.
- (62) Huang, N.; MacKerell, A. D. *J. Phys. Chem. A* **2002**, *106*, 7820–7827.
- (63) Lane, J. R.; Vaida, V.; Kjaergaard, H. G. *J. Chem. Phys.* **2008**, *128*, 034302–1–034302–11.
- (64) Donaldson, D. J. *J. Phys. Chem. A* **1999**, *103*, 62–70.
- (65) Takaoka, T.; Inamura, M.; Yanagimachi, S.; Kusunoki, I.; Komeda, T. *J. Chem. Phys.* **2004**, *121*, 4331–4338.
- (66) Babelo, D. E. *J. Phys. Chem. A* **2002**, *106*, 11190–11196.
- (67) Karthikeyan, S.; Singh, N. J.; Kim, K. S. *J. Phys. Chem. A* **2008**, *112*, 6527–6532.
- (68) Sorkin, A.; Dahlke, E. E.; Truhlar, D. G. *J. Chem. Theory Comput.* **2008**, *4*, 683–688.
- (69) Tanabe, Y.; Rode, B. M. *J. Chem. Soc., Faraday Trans. 2* **1988**, *84*, 679–692.
- (70) Ferrario, M.; Haughney, M.; McDonald, I. R.; Klein, M. L. *J. Chem. Phys.* **1990**, *93*, S156–S166.
- (71) Udomsub, S.; Hannongbua, S. J. *Chem. Soc., Faraday Trans.* **1997**, *93*, 3045–3052.
- (72) Uras, N.; Buch, V.; Devlin, J. P. *J. Phys. Chem. B* **2000**, *104*, 9203–9209.
- (73) Dang, L. X.; Garrett, B. C. *Chem. Phys. Lett.* **2004**, *385*, 309–313.
- (74) Paul, S.; Chandra, A. *J. Chem. Phys.* **2005**, *123*, 174712–1–174712–9.
- (75) Pártay, L. B.; Jedlovsky, P.; Hoang, P. N. M.; Picaud, S.; Mezei, M. *J. Phys. Chem. C* **2007**, *111*, 9407–9416.
- (76) Takenaka, N.; Koyano, Y.; Nagaoka, M. *Chem. Phys. Lett.* **2010**, *485*, 119–123.
- (77) Chakraborty, D.; Chandra, A. *J. Chem. Phys.* **2011**, *135*, 114510–1–114510–10.
- (78) Lamoureux, G.; Roux, B. *J. Chem. Phys.* **2003**, *119*, 3025–3039.
- (79) Frisch, M. J.; Trucks, G. W.; Schlegel, H. B.; Scuseria, G. E.; Robb, M. A.; Cheeseman, J. R.; Scalmani, G.; Barone, V.; Mennucci, B.; Petersson, G. A.; Nakatsuji, H.; Caricato, M.; Li, X.; Hratchian, H. P.; Izmaylov, A. F.; Bloino, J.; Zheng, G.; Sonnenberg, J. L.; Hada, M.; Ehara, M.; Toyota, K.; Fukuda, R.; Hasegawa, J.; Ishida, M.; Nakajima, T.; Honda, Y.; Kitao, O.; Nakai, H.; Vreven, T.; Montgomery, J. A., Jr.; Peralta, J. E.; Ogliaro, F.; Bearpark, M.; Heyd, J. J.; Brothers, E.; Kudin, K. N.; Staroverov, V. N.; Kobayashi, R.; Normand, J.; Raghavachari, K.; Rendell, A.; Burant, J. C.; Iyengar, S. S.; Tomasi, J.; Cossi, M.; Rega, N.; Millam, J. M.; Klene, M.; Knox, J. E.; Cross, J. B.; Bakken, V.; Adamo, C.; Jaramillo, J.; Gomperts, R.; Stratmann, R. E.; Yazyev, O.; Austin, A. J.; Cammi, R.; Pomelli, C.; Ochterski, J. W.; Martin, R. L.; Morokuma, K.; Zakrzewski, V. G.; Voth, G. A.; Salvador, P.; Dannenberg, J. J.; Dapprich, S.; Daniels, A. D.; Farkas, Ö.; Foresman, J. B.; Ortiz, J. V.; Cioslowski, J.; Fox, D. J. *Gaussian 09*, revision B.01; Gaussian, Inc.: Wallingford, CT, 2009.
- (80) Boys, S. F.; Bernardi, F. *Mol. Phys.* **1970**, *19*, S53–S66.
- (81) (a) Dunning, T. H., Jr. *J. Chem. Phys.* **1989**, *90*, 1007–1023. (b) Kendall, R. A.; Dunning, T. H., Jr.; Harrison, R. J. *J. Chem. Phys.* **1992**, *96*, 6796–6806. (c) Woon, D. E.; Dunning, T. H., Jr. *J. Chem. Phys.* **1993**, *98*, 1358–1371. (d) Dunning, T. H., Jr.; Woon, D. E.; Dunning, T. H., Jr. *J. Chem. Phys.* **1994**, *100*, 2975–2988.
- (82) Brooks, B. R.; Brooks, C. L.; Mackerell, A. D.; Nilsson, L.; Petrella, R. J.; Roux, B.; Won, Y.; Archontis, G.; Bartels, C.; Boresch, S.; Caffisch, A.; Caves, L.; Cui, Q.; Dinner, A. R.; Feig, M.; Fischer, S.; Gao, J.; Hodosscek, M.; Im, W.; Kucsera, K.; Lazaridis, T.; Ma, J.; Ovchinnikov, V.; Paci, E.; Pastor, R. W.; Post, C. B.; Pu, J. Z.; Schaefer, M.; Tidor, B.; Venable, R. M.; Woodcock, H. L.; Wu, X.; Yang, W.; York, D. M.; Karplus, M. *J. Comput. Chem.* **2009**, *30*, 1545–1614.
- (83) Lamoureux, G.; Harder, E.; Vorobyov, I. V.; Roux, B.; MacKerell, A. D. *Chem. Phys. Lett.* **2006**, *418*, 245–249.
- (84) MacKerell, A. D.; Bashford, D.; Bellott, M.; Dunbrack, R. L.; Evanseck, J. D.; Field, M. J.; Fischer, S.; Gao, J.; Guo, H.; Ha, S.; Joseph-McCarthy, D.; Kuchnir, L.; Kucsera, K.; Lau, F. T. K.; Mattos, C.; Michnick, S.; Ngo, T.; Nguyen, D. T.; Prodhom, B.; Reiher, W. E.; Roux, B.; Schlenkrich, M.; Smith, J. C.; Stote, R.; Straub, J.; Watanabe, M.; Wiorkiewicz-Kucsera, J.; Yin, D.; Karplus, M. *J. Phys. Chem. B* **1998**, *102*, 3586–3616.
- (85) Orabi, E. A.; Lamoureux, G. *J. Chem. Theory Comput.* **2012**, *8*, 182–193.
- (86) Martyna, G. J.; Tuckerman, M. E.; Tobias, D. J.; Klein, M. L. *Mol. Phys.* **1996**, *87*, 1117–1157.

- (87) Essmann, U.; Perera, L.; Berkowitz, M. L.; Darden, T.; Lee, H.; Pedersen, L. G. *J. Chem. Phys.* **1995**, *103*, 8577–8593.
- (88) Lagüe, P.; Pastor, R. W.; Brooks, B. R. *J. Phys. Chem. B* **2004**, *108*, 363–368.
- (89) Deng, Y.; Roux, B. *J. Phys. Chem. B* **2004**, *108*, 16567–16576.
- (90) Yu, H.; Whitfield, T.; Harder, E.; Lamoureux, G.; Vorobyov, I.; Anisimov, V. M.; MacKerell, A. D.; Roux, B. *J. Chem. Theory Comput.* **2010**, *6*, 774–786.
- (91) Benedict, W. S.; Gailar, N.; Plyler, E. K. *Can. J. Phys.* **1957**, *35*, 1235–1241.
- (92) Marshall, M. D.; Izgi, K. C.; Muentner, J. S. *J. Chem. Phys.* **1997**, *107*, 1037–1044.
- (93) Shimanouchi, T. *Tables of Molecular Vibrational Frequencies Consolidated*; National Bureau of Standards: Washington, DC, 1972; Vol. 1.
- (94) Haar, L.; Gallagher, J. S. *J. Phys. Chem. Ref. Data* **1978**, *7*, 635–792.
- (95) Lamoureux, G.; MacKerell, A. D.; Roux, B. *J. Chem. Phys.* **2003**, *119*, 5185–5197.
- (96) Yeh, I.-C.; Hummer, G. *J. Phys. Chem. B* **2004**, *108*, 15873–15879.
- (97) Lopes, P. E. M.; Lamoureux, G.; Roux, B.; MacKerell, A. D. *J. Phys. Chem. B* **2007**, *111*, 2873–2885.
- (98) National Bureau of Standards (U.S.), Circ. No. 142, 1923.
- (99) Lemmon, E. W.; McLinden, M. O.; Friend, D. G. Thermophysical Properties of Fluid Systems. In *NIST Chemistry WebBook*, NIST Standard Reference Database Number 69; Linstrom, P. J., Mallard, W. G., Eds.; National Institute of Standards and Technology: Gaithersburg, MD, 2000. <http://webbook.nist.gov> (retrieved March 15, 2012).
- (100) Lange, N. A. *Handbook of Chemistry*, 10th ed.; McGraw-Hill: New York, 1961.
- (101) Guevara-Carrion, G.; Vrabec, J.; Hasse, H. *Int. J. Thermophys.* **2012**, *33*, 449–468.
- (102) Idrissi, A.; Vyalov, I. *J. Phys. Chem. B* **2011**, *115*, 2011, 9646–9652.
- (103) Jones, F. M.; Arnett, E. M. *Prog. Phys. Org. Chem.* **1974**, *11*, 263–332.
- (104) Ben-Naim, A.; Marcus, Y. *J. Chem. Phys.* **1984**, *81*, 2016–2027.
- (105) King, H. H.; Hall, J. L.; Ware, G. C. *J. Am. Chem. Soc.* **1930**, *52*, 5128–5135.
- (106) Lamoureux, G.; Orabi, E. A. *Mol. Simul.* **2012**, *38*, 704–722.
- (107) Wang, S.; Orabi, E. A.; Baday, S.; Bernèche, S.; Lamoureux, G. *J. Am. Chem. Soc.* **2012**, *134*, 10419–10427.